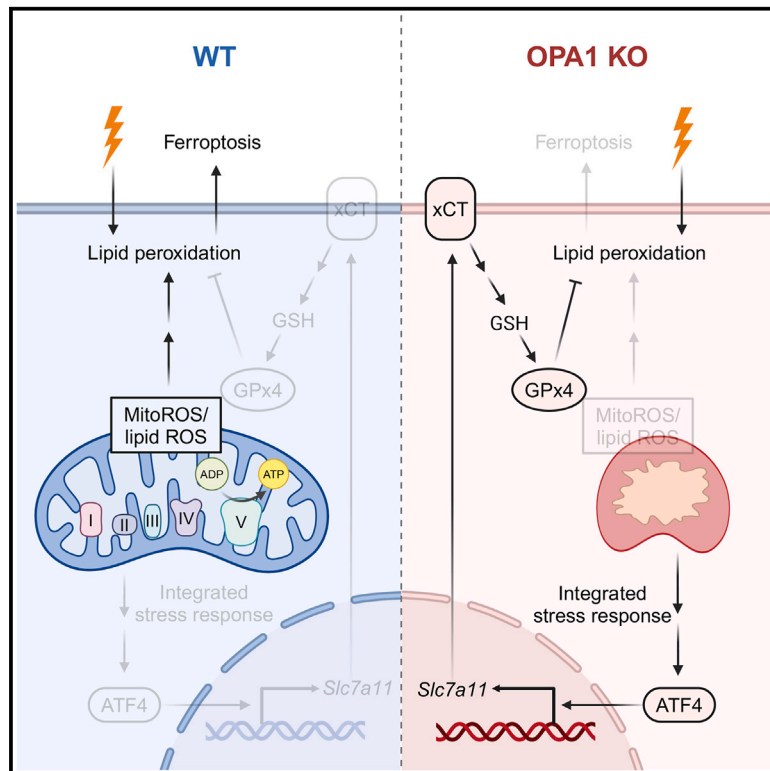


OPA1 promotes ferroptosis by augmenting mitochondrial ROS and suppressing an integrated stress response

Graphical abstract



Authors

Felix G. Liang, Fereshteh Zandkarimi, Jaehoon Lee, ..., Yisang Yoon, Brent R. Stockwell, Richard N. Kitsis

Correspondence

richard.kitsis@einsteinmed.edu

In brief

Liang et al. demonstrate that OPA1, a central mediator of mitochondrial structure and energetics, promotes ferroptotic cell death independently of its fusogenic ability. Mechanistically, OPA1 controls cellular vulnerability to ferroptosis through the modulation of mitochondrial ROS and the integrated stress response. These findings reveal an OPA1-dependent regulatory link between the mitochondrial homeostatic state and ferroptosis susceptibility.

Highlights

- OPA1 modulates cellular sensitivity to ferroptosis
- Sensitization requires OPA1's GTPase activity but not its mitochondrial fusion function
- OPA1 mediates mitochondrial ROS induction following xCT, but not GPx4, inhibition
- OPA1 suppresses an integrated stress response that inhibits ferroptosis via xCT-GPx4

Article

OPA1 promotes ferroptosis by augmenting mitochondrial ROS and suppressing an integrated stress response

Felix G. Liang,^{1,2,3} Fereshteh Zandkarimi,⁴ Jaehoon Lee,^{1,3} Joshua L. Axelrod,^{1,2,3} Ryan Pekson,^{1,3} Yisang Yoon,^{6,7} Brent R. Stockwell,^{4,5} and Richard N. Kitsis^{1,2,3,8,*}

¹Departments of Medicine, Albert Einstein College of Medicine, Bronx, NY, USA

²Departments of Cell Biology, Albert Einstein College of Medicine, Bronx, NY, USA

³Wilf Family Cardiovascular Research Institute, Albert Einstein College of Medicine, Bronx, NY, USA

⁴Department of Chemistry, Columbia University, New York, NY, USA

⁵Department of Biological Sciences, Columbia University, New York, NY, USA

⁶Department of Physiology, Medical College of Georgia, Augusta University, Augusta, GA, USA

⁷Deceased

⁸Lead contact

*Correspondence: richard.kitsis@einsteinmed.edu

<https://doi.org/10.1016/j.molcel.2024.07.020>

SUMMARY

Ferroptosis, an iron-dependent form of nonapoptotic cell death mediated by lipid peroxidation, has been implicated in the pathogenesis of multiple diseases. Subcellular organelles play pivotal roles in the regulation of ferroptosis, but the mechanisms underlying the contributions of the mitochondria remain poorly defined. Optic atrophy 1 (OPA1) is a mitochondrial dynamin-like GTPase that controls mitochondrial morphogenesis, fusion, and energetics. Here, we report that human and mouse cells lacking OPA1 are markedly resistant to ferroptosis. Reconstitution with OPA1 mutants demonstrates that ferroptosis sensitization requires the GTPase activity but is independent of OPA1-mediated mitochondrial fusion. Mechanistically, OPA1 confers susceptibility to ferroptosis by maintaining mitochondrial homeostasis and function, which contributes both to the generation of mitochondrial lipid reactive oxygen species (ROS) and suppression of an ATF4-mediated integrated stress response. Together, these results identify an OPA1-controlled mitochondrial axis of ferroptosis regulation and provide mechanistic insights for therapeutically manipulating this form of cell death in diseases.

INTRODUCTION

Ferroptosis is an iron-dependent form of oxidative cell death caused by the unchecked accumulation of lipid hydroperoxides that disrupt the integrity of cellular membranes.^{1,2} Emerging studies have implicated ferroptosis as a promising therapeutic target for the treatment of multiple degenerative diseases, ischemic syndromes, and drug-resistant cancers.^{3–5} Ferroptosis results from the imbalance between iron-dependent biochemical reactions that generate lethal lipid hydroperoxides and antioxidant mechanisms that suppress lipid peroxidation. When antioxidant defenses are compromised, membrane-incorporated phospholipids (PLs) undergo excessive Fenton-reaction-driven peroxidation, leading to membrane damage and cell death. One of the main cellular defenses against ferroptosis is glutathione peroxidase 4 (GPx4), a PL hydroperoxidase that catalyzes the reduction of oxidized lipids using glutathione (GSH) as a cofactor.^{6,7} GSH is a major cellular antioxidant required to main-

tain redox homeostasis and is essential for GPx4 function.⁸ Cysteine, the rate-limiting amino acid in GSH biosynthesis, is imported into cells in its oxidized form, cystine, through the plasma-membrane-localized cystine/glutamate antiporter known as system X_c⁻ (xCT).⁹ Decreases in cysteine abundance exhaust intracellular GSH levels, rendering GPx4 incapable of reducing cytotoxic lipid hydroperoxides.¹⁰ In addition to the xCT-GSH-GPx4 axis, CRISPR-based screens have identified GPx4-independent mechanisms centered around ferroptosis suppressor protein 1 (FSP1)^{11,12} and GTP cyclohydrolase 1 (GCH1)¹³ that utilize coenzyme Q (ubiquinone) and tetrahydrobiopterin (BH₄), respectively, as endogenous, lipophilic-radical-trapping antioxidants to protect against ferroptosis.

Execution of ferroptosis depends heavily on the intricate interplay between redox control, iron regulation, lipid metabolism, and various metabolic pathways. Although the final step in cell death may occur with disruption of plasma membrane or endoplasmic reticulum (ER) integrity by lipid hydroperoxides,

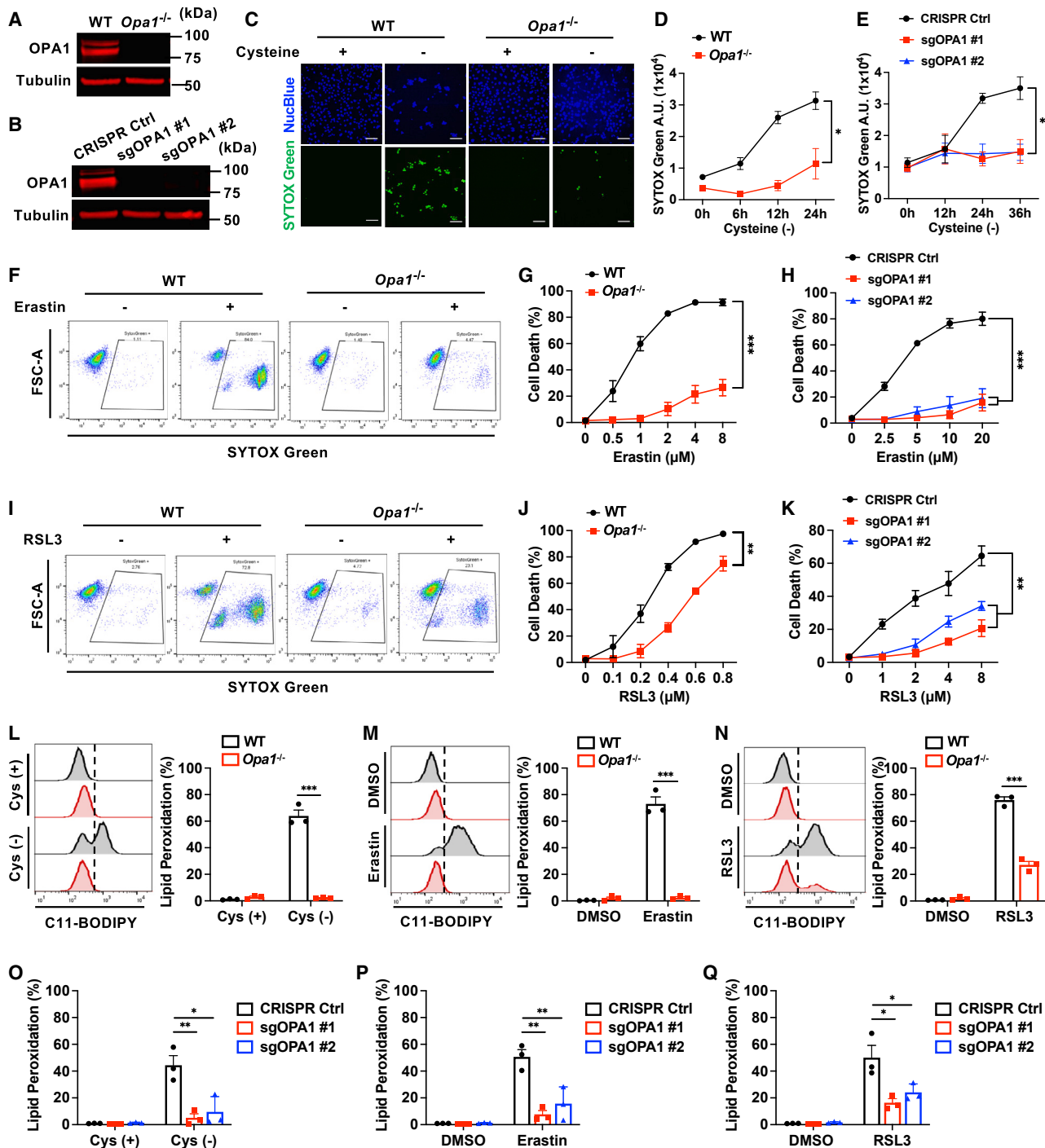


Figure 1. Loss of OPA1 protects against ferroptosis induced by cysteine deprivation, xCT inhibition, and GPx4 inhibition

(A and B) Immunoblot of OPA1 in (A) WT and *Opa1*^{-/-} MEFs and (B) control and *Opa1*-deleted U2OS cells.

(C) Representative images of WT and *Opa1*^{-/-} MEFs stained with NucBlue and SYTOX Green 24 h following cysteine withdrawal. Scale bars, 100 μm.

(D and E) Quantification of SYTOX Green signal in (D) WT and *Opa1*^{-/-} MEFs and (E) *Opa1*-deleted U2OS cells at the indicated times following cysteine deprivation.

(F) Representative flow cytometry plot of SYTOX Green in WT and *Opa1*^{-/-} MEFs treated with erastin (2 μM) for 24 h.

(G and H) Cell death quantified by SYTOX Green staining in (G) WT and *Opa1*^{-/-} MEFs and (H) *Opa1*-deleted U2OS cells treated with the indicated DMSO concentrations of erastin for 24 or 36 h, respectively.

(I) Representative flow cytometry plot of SYTOX Green in WT and *Opa1*^{-/-} MEFs treated with RSL3 (0.4 μM) for 24 h.

(legend continued on next page)

membranes of organelles, including the ER, Golgi, peroxisome, lysosome, and mitochondria, also contribute to the initiation and propagation of lipid peroxidation.^{14,15} Recently, von Krusenstiern et al., used Raman spectroscopy to confirm the ER as a primary site of lipid peroxidation during ferroptosis; however, induction of lipid reactive oxygen species (ROS) in the lysosome or mitochondria can trigger ferroptosis as well.¹⁶ As the subcellular compartment where much of the fuel substrate oxidation and oxidative phosphorylation (OXPHOS) takes place, mitochondria are a major hub for ROS generation.¹⁷ Although ROS can function as signaling molecules, high levels become cytotoxic and can induce oxidative cell death.¹⁸ Several studies have shown that inhibition of mitochondrial ROS and, particularly mitochondrial lipid ROS, can attenuate ferroptosis, suggesting that mitochondria can promote ferroptosis by directly potentiating lipid peroxidation.^{19–23} Conversely, mitochondria also possess inherent detoxification mechanisms that negatively regulate ferroptosis. Emerging studies have shown that mitochondria-localized GPx4 contributes to prevention of mitochondrial lipid peroxidation and, subsequently, ferroptosis.^{24–26} Moreover, ubiquinone synthesis and distribution, mediated by mitochondrial and cytosolic forms of steroidogenic acute regulatory protein (StAR)-related lipid transfer domain protein 7 (STARD7), respectively, provide protection against ferroptosis.²⁷

Optic atrophy 1 (OPA1) is a dynamin-like GTPase localized to the inner mitochondrial membrane (IMM) that mediates mitochondrial fusion, respiratory supercomplex assembly, cristae remodeling, mitochondrial DNA maintenance, and energetics.^{28,29} Given the critical role of OPA1 in controlling mitochondrial structure and energetics, we posited that OPA1 may serve as a nodal point of ferroptosis regulation through modulation of mitochondria-dependent mechanisms. Indeed, we found that loss of OPA1 markedly suppresses ferroptosis in both mouse and human cells. Although the GTPase activity of OPA1 is required for its ability to drive ferroptosis, its mitochondrial fusion function is dispensable. Instead, loss of OPA1 promotes a ferroptosis-resistant state by attenuating mitochondrial lipid ROS generation and inducing an activating transcription factor 4 (ATF4)-dependent upregulation of the xCT-GSH-GPx4 pathway as part of the integrated stress response. Collectively, these findings establish OPA1 as an important regulator of ferroptosis and reveal a key mitochondrial axis for control of this cell death program.

RESULTS

Loss of OPA1 suppresses lipid peroxidation and ferroptotic cell death

To study the role of OPA1 in ferroptosis, we utilized mouse embryonic fibroblasts (MEFs) and human U2OS osteosarcoma

cells. Loss of OPA1 in MEFs derived from germline *Opa1*^{-/-} mice and U2OS cells subjected to CRISPR-mediated excision was confirmed by western blotting (Figures 1A and 1B). Ferroptosis was induced by inactivating GPx4-dependent defense mechanisms using three different approaches. First, we subjected wild-type (WT) and OPA1-deficient MEFs and U2OS cells to cysteine deprivation, which depletes intracellular GSH, an essential cofactor of GPx4. Cell death was scored by loss of plasma membrane integrity using SYTOX Green, a membrane-impermeable dye. Although cysteine deprivation induced loss of plasma membrane integrity in WT cells, this was markedly reduced in OPA1-deficient cells (Figure 1C). Quantification of the SYTOX Green signal using a fluorescence plate reader demonstrated that cells lacking OPA1 are protected from cysteine-deprivation-induced ferroptosis over the course of 24–36 h (Figures 1D and 1E).

Next, we tested whether MEFs and U2OS cells depleted of OPA1 are protected against ferroptosis induced by small molecules erastin and RAS-selective lethal 3 (RSL3), which inhibit xCT and GPx4, respectively. Cell death was assessed by SYTOX Green using flow cytometry. Loss of OPA1 conferred resistance against erastin-induced (Figures 1F–1H) and RSL3-induced (Figures 1I–1K) ferroptosis across a broad range of concentrations, although protection from erastin was noticeably greater than that from RSL3. Because lipid peroxidation is the hallmark and driver of ferroptotic cell death, we also measured lipid peroxidation in these cells by flow cytometry using the C-11 BODIPY dye. Consistent with the cell death results, cells depleted of OPA1 exhibit markedly reduced levels of lipid peroxidation upon cysteine deprivation, erastin treatment, or RSL3 treatment (Figures 1L–1Q). Taken together, these results demonstrate that loss of OPA1 reduces lipid peroxidation and cell death triggered by multiple inducers of ferroptosis, suggesting that OPA1 is a positive regulator of this form of cell death.

GTPase activity is required for sensitization of cells to ferroptosis by OPA1

OPA1 GTPase activity is required for its regulation of mitochondrial structure, fusion, and oxidative phosphorylation.^{30–32} Accordingly, we next investigated whether OPA1 GTPase activity is also required for the promotion of ferroptosis by OPA1. To address this, we reconstituted *Opa1*^{-/-} MEFs with retroviral constructs that express either WT or K301A human OPA1, the latter being a GTPase-defective mutant.³¹ Immunoblotting showed similar expression levels of WT OPA1 and K301A OPA1 in reconstituted cells (Figure 2A). Consistent with its loss of GTPase activity, the K301A mutant was unable to restore fused mitochondrial morphology in *Opa1*^{-/-} MEFs (Figures 2B and 2C). Next, we subjected these *Opa1*^{-/-} MEFs cells that stably express WT OPA1 or K301A OPA1 to conditions that induce

(J and K) Cell death quantified by SYTOX Green staining in (J) WT and *Opa1*^{-/-} MEFs and (K) *Opa1*-deleted U2OS cells treated with the indicated concentrations of RSL3 for 24 or 36 h, respectively.

(L–N) Lipid peroxidation quantified using C-11 BODIPY staining in WT and *Opa1*^{-/-} MEFs following (L) cysteine deprivation, (M) erastin (2 μ M) treatment, or (N) RSL3 (0.4 μ M) treatment for 8 h.

(O–Q) Lipid peroxidation quantified using C-11 BODIPY staining in *Opa1*-deleted U2OS cells following (O) cysteine deprivation, (P) erastin (10 μ M) treatment, or (Q) RSL3 (4 μ M) treatment for 16 h. All data represent mean \pm SEM; $n = 3$ independent experiments. Statistical analysis was performed using unpaired, two-tailed Student's t test or one-way ANOVA. * $p < 0.05$, ** $p < 0.01$, *** $p < 0.001$.

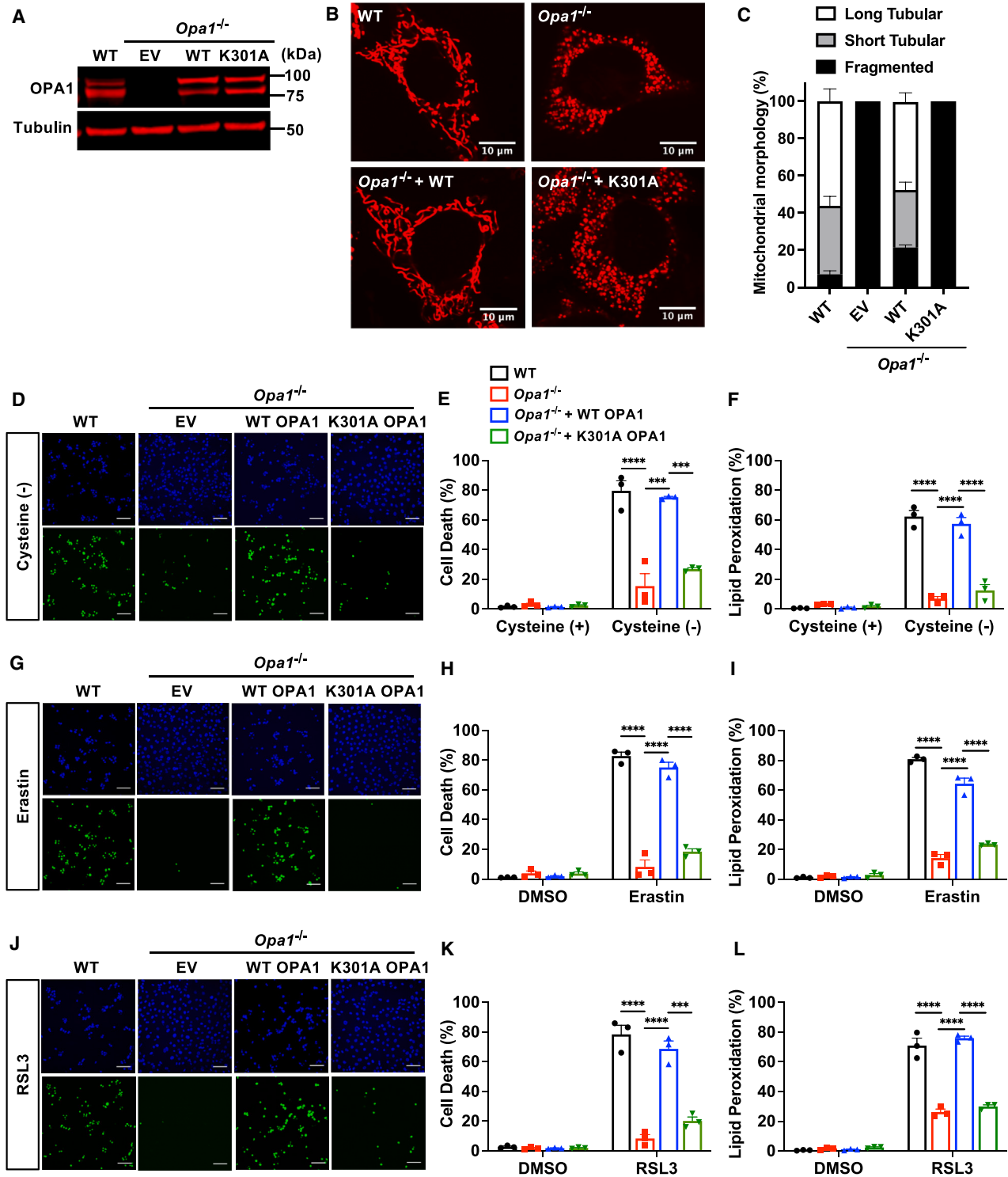


Figure 2. GTPase activity is important for OPA1-mediated ferroptosis

(A) Immunoblot of OPA1 in indicated MEF cell lines.

(B) Representative images showing mitochondria stained with MitoTracker Deep Red in indicated MEF cell lines.

(C) Mitochondrial morphologies were categorized into long tubular, short tubular, or fragmented mitochondria and scored in the indicated MEF cell lines.

(D, G, and J) Representative images of indicated MEF cell lines stained with NucBlue and SYTOX Green following (D) cysteine deprivation, (G) erastin (2 μM) treatment, or (J) RSL3 (0.4 μM) treatment for 24 h. Scale bars, 100 μm.

(legend continued on next page)

ferroptosis, using cysteine deprivation, erastin, or RSL3 treatment. In all three cases, we observed that WT OPA1, but not the K301A OPA1 mutant, was able to restore cell death and lipid peroxidation to *Opa1*^{-/-} MEFs (Figures 2D–2L), indicating that the GTPase activity is critical for the promotion of ferroptosis by OPA1.

OPA1 promotion of ferroptosis occurs independently of mitochondrial fusion

Mitochondria undergo dynamic cycles of fusion and fission to maintain quality control and adapt to fluctuations in cellular conditions. Modulation of mitochondrial dynamics can impact cell proliferation, inflammation, ROS signaling, Ca²⁺ handling, lipid transfer, and cell death.^{29,33} Independent groups have shown that treatment of cells with ferroptosis inducers erastin or RSL3 can induce mitochondrial fragmentation,^{20,34,35} but the role of mitochondrial dynamics has not been evaluated extensively in ferroptosis. As OPA1 mediates fusion of the IMM, we asked whether this function is important in its promotion of ferroptosis.

In humans, *Opa1* gives rise to at least 8 alternatively spliced transcripts that are differentially expressed in various tissues.^{36,37} These isoforms can undergo full or partial proteolytic cleavage to generate an IMM-bound long form of OPA1 (L-OPA1) or a short, soluble form of OPA1 (S-OPA1) that resides in the space between the outer mitochondrial membrane and IMM.²⁸ The L and S forms of OPA1 can cooperate to promote mitochondrial fusion.³⁸ However, while L-OPA1 alone has some fusogenic activity, S-OPA1 alone is fusion incompetent.^{31,32}

To investigate the role of mitochondrial fusion in the sensitization of ferroptosis by OPA1, we employed a cellular model in which *Opa1*^{-/-} MEFs were engineered to express both L- and S-OPA1, L-OPA1 alone, or S-OPA1 alone (Figures 3A and 3B). This was achieved by stably reconstituting *Opa1*^{-/-} MEFs with various OPA1 constructs. Reconstitution with OPA1 isoform 1, which is partially cleaved at the S1 site, was used to express both L- and S-OPA1. OPA1 isoform 1 with the S1 site deleted was used to express only L-OPA1. OPA1 isoform 5, which undergoes full cleavage at S3 site, was employed to express only S-OPA1. Consistent with previous work,^{31,32} mitochondrial fusion was fully rescued in cells expressing both L- and S-OPA1, while a partial rescue resulted from expression of L-OPA1 alone (Figures 3C and 3D). In contrast, S-OPA1 was unable to restore mitochondrial interconnectivity (Figures 3C and 3D).

Next, we subjected these reconstituted cells to ferroptosis induced by cysteine deprivation, erastin, or RSL3 treatment. If the ability to promote mitochondrial fusion were important in sensitization to ferroptosis by OPA1, one would predict that sensitization would be most marked in *Opa1*^{-/-} MEFs reconstituted to express both L-OPA1 and S-OPA1 and would be minimal in cells expressing S-OPA1 alone. In contrast, we observed

similar magnitudes of cell death in each of these cell lines in response to each of the ferroptosis stimuli (Figures 3E–3J). Similarly, levels of lipid peroxidation induced during ferroptosis were similar among the reconstituted cell lines (Figures 3K–3M). These data indicate that the ability of OPA1 to sensitize cells to ferroptosis is independent of its ability to promote mitochondrial fusion, despite the fact that both processes require OPA1 GTPase activity.

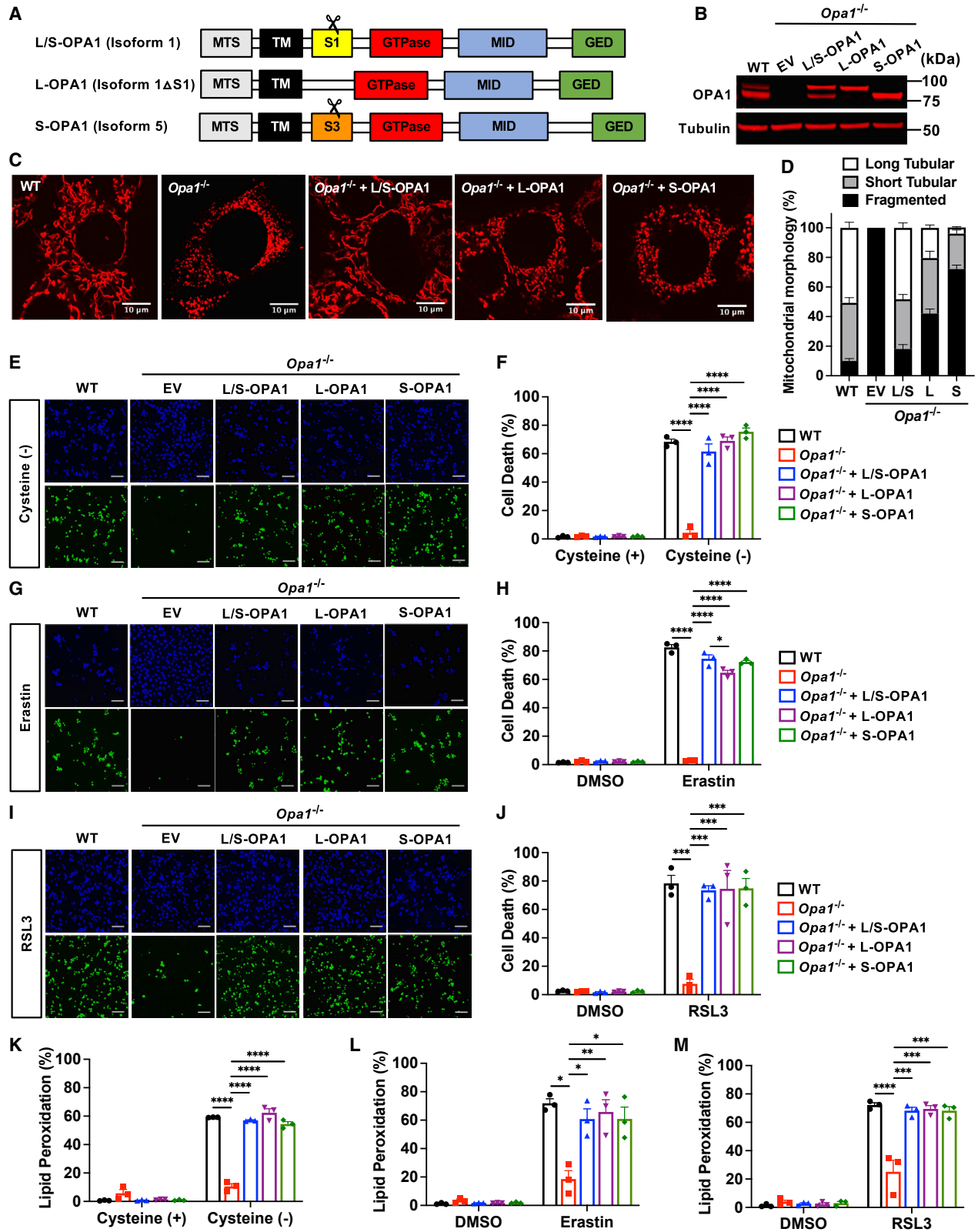
Contribution of OPA1-mediated mitochondrial structure and energetics to the generation of mitochondrial ROS and lipid ROS during ferroptosis

In addition to mediating mitochondrial fusion, OPA1 is also a regulator of cristae ultrastructure, electron transport chain (ETC) complex assembly, and oxidative phosphorylation.^{29,39} Unlike mitochondrial fusion, however, L-OPA1 and S-OPA1 are individually capable of supporting cristae morphology, super-complex integrity, and mitochondrial respiration.³⁹ We first confirmed that OPA1 deficiency results in cristae disorganization (Figure 4A) and impaired assembly of mitochondrial respiratory complexes I, III, IV, and V, but not complex II (Figures 4B–4F). Expression of L-OPA1, S-OPA1, or both was able to rescue the cristae structure and complex assembly defects (Figures 4A–4F). As expected, *Opa1*^{-/-} MEFs also exhibited decreases in oxygen consumption rate (OCR), which were partially rescued by expression of L-OPA1, S-OPA1, or both (Figures 4G and 4H).

The ETC is a major source of ROS production in the mitochondria. Given that previous studies have implicated mitochondrial ROS and mitochondrial lipid ROS as potentiators of ferroptosis, we investigated the role of OPA1 in mediating these oxidative changes during ferroptosis. Mitochondrial ROS was assessed using MitoSox, a commonly used sensor for mitochondrial superoxide, and MitoPerOx, a mitochondria-targeted BODIPY probe, was used to assess mitochondrial lipid ROS. Because increases in mitochondrial membrane potential have previously been shown to occur during ferroptosis,⁴⁰ we first confirmed that changes in MitoSox and MitoPerOx signals were not merely reflective of changes in mitochondrial membrane potential. We observed that co-treatment of WT cells with ferrostatin-1 (Fer-1) suppressed erastin-induced increases in mitochondrial ROS (Figure S1A) and mitochondrial lipid ROS (Figure S1B) without affecting mitochondrial membrane potential (Figure S1C). This result indicates that MitoSox and MitoPerOx are indeed measuring changes in mitochondrial ROS and lipid ROS independently of membrane potential. Using these validated chemical sensors, we found that cysteine deprivation and erastin treatment induce mitochondrial ROS and mitochondrial lipid ROS in WT cells, but not in *Opa1*^{-/-} MEFs cells (Figures 4I–4L). Re-expression of L-OPA1, S-OPA1, or both in *Opa1*^{-/-} MEFs restored ROS production following cysteine deprivation and erastin treatment (Figures 4I–4L). In contrast, OPA1 loss did not prevent accumulation of mitochondrial ROS or mitochondrial lipid

(E, H, and K) Cell death quantified by SYTOX Green staining in the indicated MEF cell lines following (E) cysteine deprivation, (H) erastin (2 μ M) treatment, or (K) RSL3 (0.4 μ M) treatment for 24 h.

(F, I, and L) Lipid peroxidation quantified using C-11 BODIPY staining in indicated MEF cell lines following (F) cysteine deprivation, (I) erastin (2 μ M) treatment, or (L) RSL3 (0.4 μ M) treatment for 8 h. All data represent mean \pm SEM; $n = 3$ independent experiments. Statistical analysis was performed using one-way ANOVA. * $p < 0.05$, ** $p < 0.01$, *** $p < 0.001$, **** $p < 0.0001$.



(legend on next page)

ROS with direct GPx4 inhibition by RSL3 (Figures S2A and S2B). These findings demonstrate that the accumulation of mitochondrial ROS and lipid ROS induced by deficient cysteine importation (whether resulting from cysteine deprivation or xCT inhibition) is OPA1-dependent, while the accumulation of mitochondrial ROS and lipid ROS induced by GPx4 inhibition is independent of OPA1. This differential dependence of mitochondrial ROS and mitochondrial lipid ROS accumulation on OPA1 may explain why *Opa1*^{-/-} MEFs are more resistant to ferroptosis induced by erastin compared with RSL3 (Figures 1G and 1J).

Upregulation of the xCT-GSH-GPx4 pathway mediates ferroptosis resistance in OPA1-depleted cells

Despite differences in the magnitude of the effect, OPA1 deficiency nevertheless confers resistance to RSL3-induced ferroptosis as well as to erastin-induced ferroptosis. For this reason, we sought additional mechanisms by which OPA1 deficiency mediates this resistance and their applicability to cysteine-deprivation-, erastin-, and RSL3-induced ferroptosis. Because the xCT-GSH-GPx4 pathway is a central defense mechanism that abrogates accumulation of lethal lipid peroxides and subsequent ferroptotic cell death, we assessed whether this pathway is altered with OPA1 loss. We found that *Slc7a11*, the gene that encodes xCT, is transcriptionally upregulated in both OPA1-depleted MEFs (Figure 5A) and U2OS cells (Figure 5B) and that glutamate release, an indicator of xCT activity, is also increased in these cells at baseline (Figures 5C and 5D). Both of these changes were reversed by re-expression of OPA1 in *Opa1*^{-/-} MEFs. Cysteine is the rate-limiting amino acid required for synthesis of GSH, which serves as an essential cofactor for GPx4 function. Consistent with increases in xCT activity and, therefore, cysteine uptake, we detected increased levels of GSH in OPA1-depleted MEFs and U2OS cells at baseline, which remained elevated upon erastin treatment (Figures 5E and 5F). In addition to elevated GSH pools, cells lacking OPA1 also had higher levels of GPx4 protein (Figures 5G and 5H), which were not attributable to changes in transcription (Figures S3A and S3B). Reductions in GPx4 protein abundance during ferroptosis have been shown to be mediated by decreases in translation and/or protein stability.^{41–44} Similarly, we observed a time-dependent decrease in GPx4 levels during erastin and RSL3 treatment. Importantly, however, GPx4 levels remained higher in OPA1-depleted cells compared with WT cells over the time course of ferroptosis, consistent with GPx4 contributing to resistance to killing in response to both stimuli (Figures 5I and 5J). To test whether in-

creases in xCT in OPA1-depleted cells is responsible for conferring ferroptosis resistance, we used two independent short hairpin RNAs (shRNAs) to knockdown *Slc7a11* transcripts in *Opa1*^{-/-} MEFs to levels comparable to those in WT MEFs (Figure 5K). Upon *Slc7a11* knockdown, *Opa1*^{-/-} MEFs became susceptible to erastin-induced ferroptosis (Figures 5L and 5M) and, interestingly, to RSL3-induced ferroptosis as well (Figures 5N and 5O). It is understandable that, by decreasing cysteine uptake and GSH levels, *Slc7a11* knockdown would resensitize *Opa1*^{-/-} MEFs to erastin-induced ferroptosis. However, given that RSL3 induces ferroptosis by directly inhibiting GPx4, which is downstream of GSH depletion, it was not immediately clear why *Slc7a11* knockdown would also restore RSL3-induced ferroptosis in *Opa1*^{-/-} MEFs. A previous study showed that cysteine availability is coupled to GPx4 translation and that limiting cysteine can decrease GPx4 protein levels, thereby exacerbating RSL3-induced ferroptosis.⁴¹ To this end, we immunoblotted for GPx4 and found that increases in GPx4 protein levels in *Opa1*^{-/-} MEFs were reversed with *Slc7a11* knockdown (Figure S3C). Together, these data reveal that upregulation of the xCT-GSH-GPx4 pathway with OPA1 loss is important to resistance to ferroptosis induced by both xCT or GPx4 inhibition.

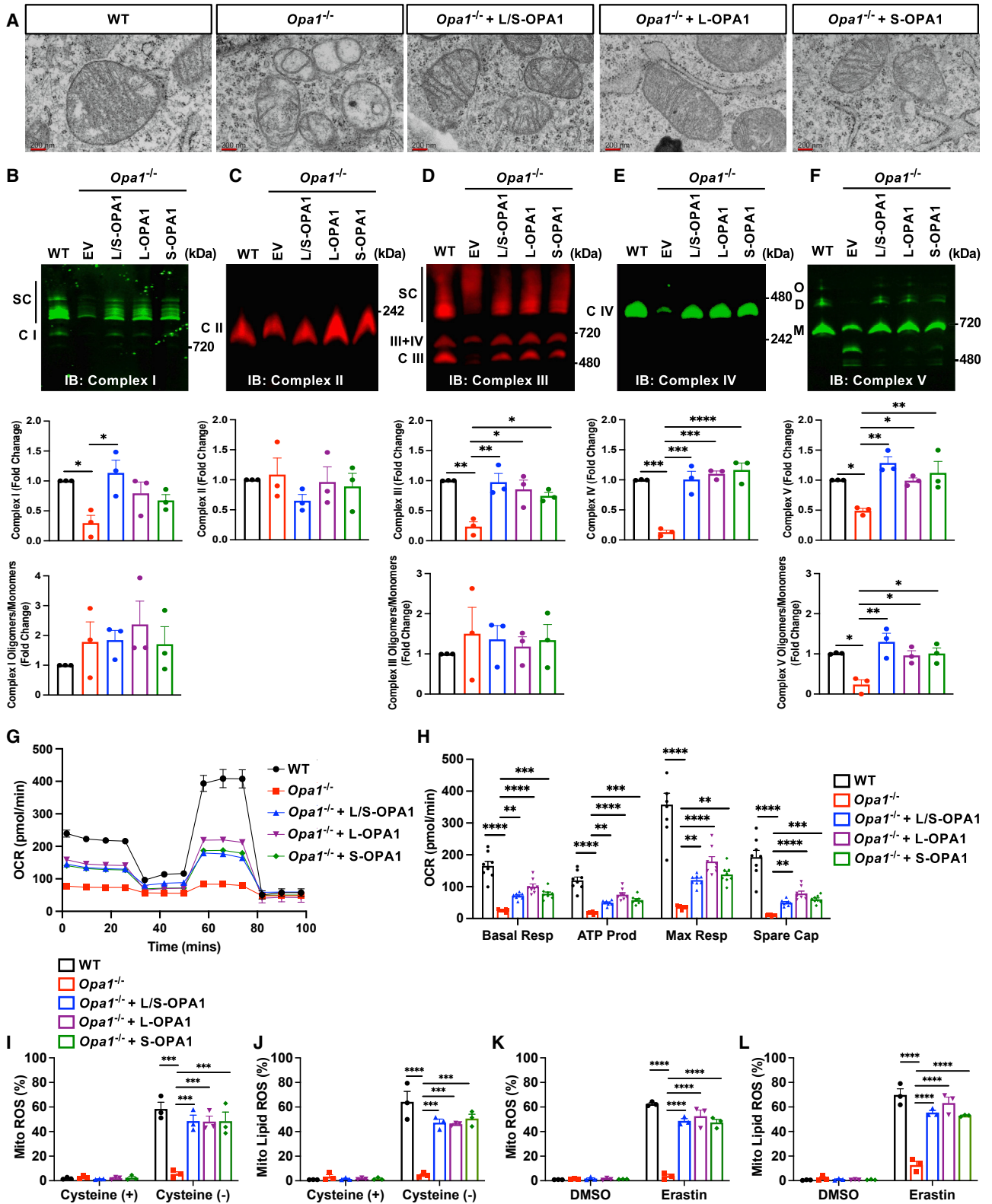
Along with the xCT-GSH-GPx4 pathway, coenzyme Q (ubiquinone)-mediated mechanisms provide another major cellular defense against ferroptosis. However, immunoblotting showed no difference in levels of ubiquinone-related proteins, FSP1, dihydroorotate dehydrogenase (DHODH), and STARD7, between WT and *Opa1*^{-/-} MEFs at baseline or when treated with erastin or RSL3 (Figures S4A and S4B). Moreover, levels of CoQ10, a predominant form of coenzyme Q, were also unchanged (Figure S4C). These results indicate that CoQ-mediated mechanisms are unlikely to be involved in ferroptosis resistance conferred by OPA1 loss.

Induction of ATF4-dependent integrated stress response is necessary for the ferroptosis-resistant state of OPA1-depleted cells

To gain insight into the link between OPA1 loss and transcriptional upregulation of *Slc7a11*, we performed RNA sequencing (RNA-seq) on *Opa1*^{-/-} MEFs and *Opa1*^{-/-} MEFs reconstituted with OPA1. RNA-seq analysis of these two otherwise isogenic cell populations using 4 replicates per group revealed approximately 740 genes that were differentially expressed (Figures S5A and S5B). Ingenuity pathway analysis (IPA) identified numerous enriched signaling pathways, including mitochondrial

Figure 3. OPA1 regulates ferroptosis independently of mitochondrial fusion

(A) Schematic of OPA1 variants expressed in *Opa1*^{-/-} MEFs. MTS, mitochondrial targeting sequence; TM, transmembrane domain; S1, S1 cleavage site; S3, S3 cleavage site; MID, middle domain; GED, GTPase effector domain.
(B) Immunoblot of OPA1 in indicated MEF cell lines.
(C) Representative images showing mitochondria stained with MitoTracker Deep Red in indicated MEF cell lines.
(D) Mitochondrial morphologies were categorized into long tubular, short tubular, or fragmented mitochondria and scored in the indicated MEF cell lines.
(E, G, and I) Representative images of the indicated MEF cell lines stained with NucBlue and SYTOX Green following (E) cysteine deprivation, (G) erastin (2 μ M) treatment, or (I) RSL3 (0.4 μ M) treatment for 24 h. Scale bars, 100 μ m.
(F, H, and J) Cell death quantified by SYTOX Green staining in the indicated MEF cell lines following (F) cysteine deprivation, (H) erastin (2 μ M) treatment, or (J) RSL3 (0.4 μ M) treatment for 24 h.
(K, L, and M) Lipid peroxidation quantified using C-11 BODIPY staining in the indicated MEF cell lines following (K) cysteine deprivation, (L) erastin (2 μ M) treatment, or (M) RSL3 (0.4 μ M) treatment for 8 h. All data represent mean \pm SEM; $n = 3$ independent experiments. Statistical analysis was performed using one-way ANOVA. * $p < 0.05$, ** $p < 0.01$, *** $p < 0.001$, **** $p < 0.0001$.



(legend on next page)

dysfunction and GSH-redox pathways (Figure S5C). Further unbiased analysis of upstream transcriptional regulators of differentially expressed genes revealed several candidates previously reported in an *Opa1*-deleted context, including ATF4 and nuclear factor κ B (NF- κ B),^{45,46} and also unreported candidates including SOX4 and KLF4 (Figure 6A). Among the top transcriptional regulators, ATF4, which possessed the highest activation Z score and one of the highest false discovery rate (FDR) scores (Figures 6A and 6B), is of particular interest due to its previously reported relationship to both OPA1^{45,47} and ferroptosis.^{48–50} ATF4 is a key transcriptional activator of the integrated stress response, which facilitates cellular adaptation to diverse stresses, including mitochondrial dysfunction.^{51,52} Differentially expressed genes predicted to be upregulated by ATF4 include canonical ATF4-target genes *Chac1*, *Ddit4*, *Fgf21*, and *Slc1a4*^{52,53} as well as genes related to ferroptosis resistance, including *Slc7a11*, *Cth*, and *Psph*^{54,55} (Figure 6C). Accordingly, we next examined whether ATF4 abundance is increased in MEFs and U2OS cells depleted of OPA1.

ATF4 abundance is translationally upregulated during the integrated stress response by bypassing of its upstream inhibitory open reading frames when global translation is impaired by phosphorylation of eukaryotic initiation factor 2 α (eIF2 α). Immunoblot analysis of OPA1-depleted MEFs and U2OS cells indeed showed increases in the abundance of phosphorylated eIF2 α and ATF4 (Figures 6D and 6E). To assess the ATF4 dependence of increases in the expression of putative target genes in response to OPA1 depletion, we depleted ATF4 using two independent shRNAs (Figure 6F). Knockdown of ATF4 reversed increases in the expression of *Slc7a11*, *Cth*, *Fgf21*, and *Psph*, each encoding a negative regulator of ferroptosis (Figure 6G). Further, knockdown of ATF4 resensitized *Opa1*^{-/-} MEFs to ferroptosis in response to erastin and RSL3 (Figures 6H–6K). In contrast to the ATF4-dependent induction of *Slc7a11* in *Opa1*^{-/-} cells, knockdown of *Slc7a11* did not affect activation of the integrated stress response and increases in ATF4 in cells lacking OPA1, suggesting that the regulation between ATF4 and xCT is not bidirectional (Figure S6). In summary, these data demonstrate that an ATF4-dependent integrated stress response, resulting in the upregulation of multiple negative regulators of ferroptosis, is critical for resistance to both erastin- and RSL3-induced ferroptosis conferred by loss of OPA1.

Mitochondrial stress can be relayed by the OMA1-DELE1-HRI pathway to induce ATF4 activation.⁵⁶ To assess whether this signaling cascade is responsible for activating the integrated stress response in the absence of OPA1, we knocked down *Oma1*, *Dele1*, and *Hri* individually in *Opa1*^{-/-} MEFs (Figure S7A)

and found a reduction in the level of *Slc7a11* transcripts (Figure S7B). Protein levels of phosphorylated eIF2 α , ATF4, and GPX4 were also decreased in these cells (Figure S7C). As with ATF4 knockdown, genetic inhibition of the OMA1-DELE1-HRI pathway resensitized *Opa1*^{-/-} MEFs to erastin- and RSL3-induced ferroptosis (Figures S7D–S7G).

OPA1 deficiency significantly alters global lipid profile

Lipids play vital roles in forming the building blocks of cellular membranes, acting as signaling molecules and participating in energy metabolism.⁵⁷ In addition to functionally interacting with lipids within the IMM,⁵⁸ OPA1 has been shown to directly or indirectly influence lipid metabolism.^{59–61} To identify the impact of OPA1 on global lipid signatures, we performed untargeted mass spectrometry-based lipidomics on WT and *Opa1*^{-/-} MEFs. This approach allowed us to detect approximately 200 lipid species whose levels were differentially altered, which we categorized into the following classes: PLs, lyso-PLs (lysoPLs), glycerolipids (GLs), free fatty acids (FAs), and sphingolipids (SpLs). PL levels were most differentially altered with changes observed in both directions with *Opa1* loss (Figure 7A). During ferroptosis, polyunsaturated FA-containing PLs (PUFA-PLs), in particular, are known to be highly susceptible to peroxidation due to the bis-allylic hydrogen that is flanked by double-bonded carbons and, thereby, provide the necessary substrates for generation of lipid peroxides.^{62,63} Conversely, monounsaturated FA-containing PLs (MUFA-PLs) reduce accumulation of lipid ROS at the plasma membrane.⁶⁴ Accordingly, we further differentiated the PLs into PUFA-PLs and MUFA-PLs (Figures 7B and 7C) to better characterize the differences within these subclasses. In the PUFA-PLs, we observed species that are both enriched and depleted in the *Opa1*^{-/-} MEFs (Figure 7B). Similarly, this was also true for the lysoPLs, the byproducts of oxidized PLs (Figure S8A). On the other hand, the majority of differentially altered MUFA-PLs were significantly enriched in the *Opa1*^{-/-} MEFs (Figure 7C), suggesting that the accumulation of MUFA-PLs may also have a potential role in ferroptosis suppression. Like MUFA-PLs, GLs, free FAs, and SpLs were also enriched in the *Opa1*^{-/-} MEFs (Figures S8B–S8D).

DISCUSSION

OPA1 is a ubiquitously expressed protein that plays important roles in regulating mitochondrial structure, genomic integrity, OXPHOS, and interconnectivity.³⁹ In this study, we demonstrate that OPA1 plays a critical role in sensitizing cells to ferroptosis and elucidate underlying mechanisms. This effect of OPA1 on

Figure 4. OPA1 regulates levels of mitochondrial ROS and mitochondrial lipid ROS during cysteine-deprivation- and erastin-induced ferroptosis

(A) Electron microscopy images of mitochondrial cristae in indicated MEF cell lines. Scale bars, 200 nm.

(B–F) Immunoblots and quantifications of BN-PAGE showing (B) complex I, (C) complex II, (D) complex III, (E) complex IV, and (F) complex V levels in the indicated MEF cell lines. SC, supercomplex; o, oligomer; d, dimer; m, monomer.

(G) Cellular oxygen consumption rates (OCRs) measured using Seahorse extracellular flux analysis in the indicated MEF cell lines.

(H) OCR parameters, including basal respiration, ATP production, maximal respiration, and spare capacity. Data represent mean \pm SEM; $n = 8$ wells per group.

(I and J) (I) Mitochondrial ROS quantified using MitoSox staining and (J) mitochondrial lipid peroxidation, quantified using MitoPerOx staining in the indicated MEF cell lines following cysteine deprivation for 8 h.

(K and L) (K) Mitochondrial ROS and (L) mitochondrial lipid peroxidation in the indicated MEF cell lines treated with erastin (2 μ M) for 8 h. Data represent mean \pm SEM; $n = 3$ independent experiments. Statistical analysis was performed using one-way ANOVA. * $p < 0.05$, ** $p < 0.01$, *** $p < 0.001$, **** $p < 0.0001$.

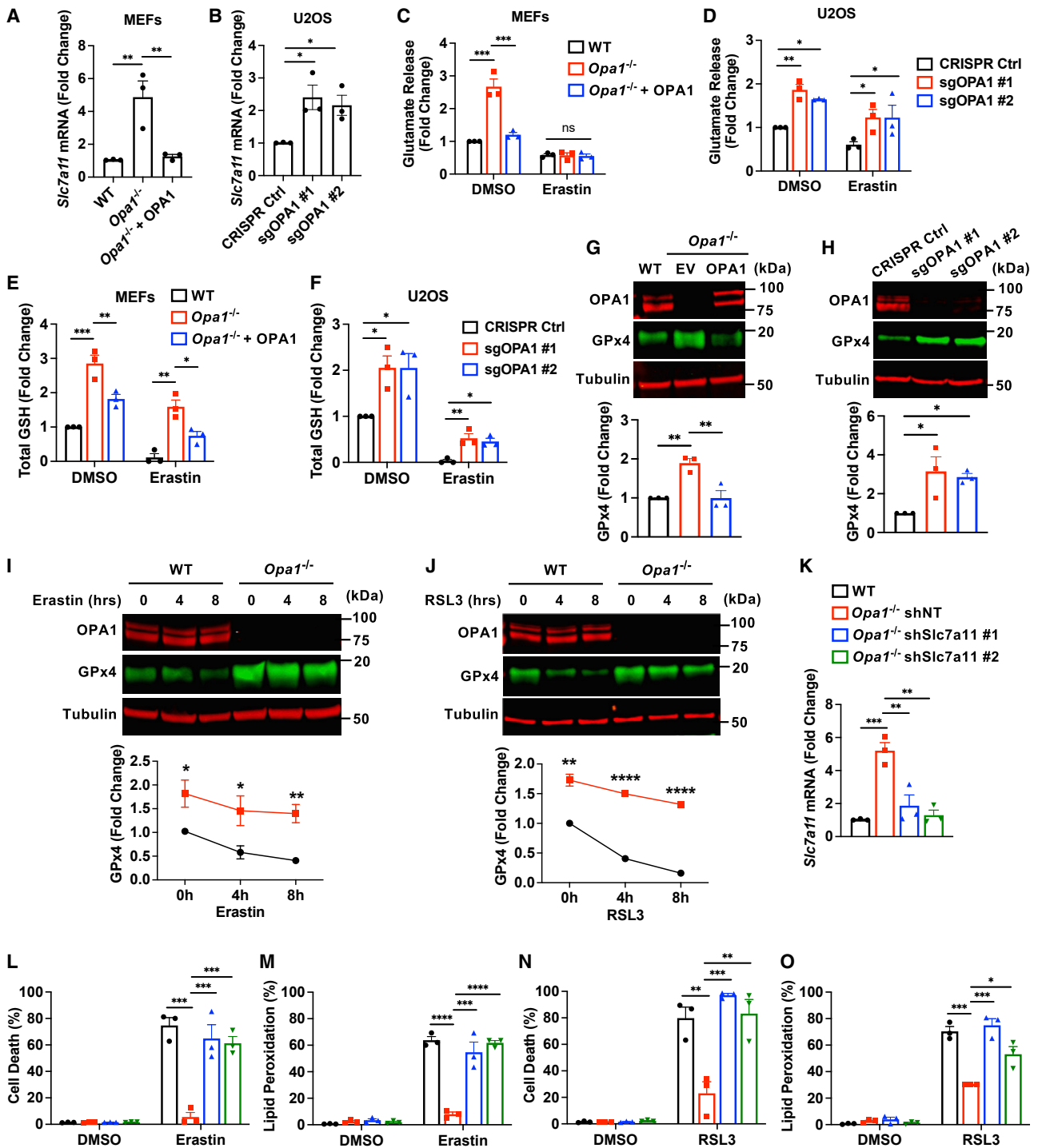


Figure 5. Loss of OPA1 upregulates the xCT-GSH-GPx4 pathway to suppress erastin- and RSL3-induced ferroptosis

(A–D) *Slc7a11* mRNA levels in the indicated (A) MEFs and (B) U2OS cells. Glutamate release assay in the indicated (C) MEFs and (D) U2OS cells untreated or treated with erastin.

(E and F) Total glutathione levels in the indicated (E) MEFs and (F) U2OS cells not treated or treated with erastin.

(G and H) Immunoblot of GPx4 levels in the indicated (G) MEFs and (H) U2OS cells.

(I and J) Immunoblot of GPx4 levels in WT and *Opa1*^{-/-} MEFs treated with (I) erastin (2 μ M) and (J) RSL3 (0.4 μ M) for indicated times.

(K) *Slc7a11* mRNA levels following shRNA-mediated knockdown in *Opa1*^{-/-} MEFs.

(legend continued on next page)

ferroptosis is directionally opposite to its cytoprotective role in apoptosis,^{65,66} a finding that highlights the complex roles of mitochondria as mediators of distinct forms of cell death.

Given that OPA1 GTPase activity is vital in controlling mitochondrial shape and function, we investigated whether this GTPase activity is needed for OPA1 to sensitize cells to ferroptosis. Ferroptosis susceptibility was restored to *Opa1*^{-/-} MEFs by reconstitution of WT OPA1, but not the GTPase-inactive K301A mutant, demonstrating that the GTPase activity is, in fact, important for this function. Because OPA1 GTPase activity is also critical for the ability of OPA1 to mediate IMM events during mitochondrial fusion, we postulated that increases in mitochondrial interconnectivity may be important for the sensitization of ferroptosis by OPA1. However, our analysis of OPA1 mutants with differential abilities to support mitochondrial fusion, all of which were GTPase competent, demonstrated that the promotion of mitochondrial fusion is not required for OPA1 to sensitize cells to ferroptosis.

Mitochondrial ROS and lipid ROS contributes to the initiation and execution of ferroptosis.^{16,21,25} We found that loss of OPA1 markedly decreased mitochondrial ROS and lipid ROS accumulation in response to cysteine deprivation or xCT inhibition by erastin, correlating with changes in cristae structure, ETC complexes, and mitochondrial respiration. However, the accumulation of mitochondrial ROS and lipid ROS in response to GPx4 inhibition with RSL3 was independent of OPA1, which could explain why loss of OPA1 does not protect from GPx4 inhibition as completely as from cysteine deprivation or xCT inhibition. Further, these observations suggest that cysteine deprivation/xCT inhibition and RSL3 inhibition induce accumulation of mitochondrial superoxide and lipid peroxides through distinct mechanisms. Additionally, our results offer a potential explanation for the findings of Gao et al. demonstrating that inhibition of mitochondrial ETC activity or tricarboxylic acid cycle blocks only cysteine deprivation/xCT-inhibition-induced ferroptosis, but not GPx4-inhibition-induced ferroptosis.⁴⁰ Further investigation will be needed to understand the various mechanisms by which cysteine deprivation/xCT inhibition versus Gpx4 inhibition promote the accumulation of mitochondrial ROS and lipid ROS in ferroptosis.

OPA1 loss, in addition to preventing generation of mitochondrial lipid ROS, results in upregulation of a central ferroptosis defense mechanism—the xCT-GSH-GPx4 pathway. We found that xCT is transcriptionally upregulated in OPA1-depleted MEFs and U2OS cells, and others have reported this same observation in OPA1-deficient multipotent stem cells.^{67,68} The increased xCT-mediated cysteine uptake results in elevated levels of GSH that enable the peroxidase activity of GPx4, thereby attenuating cysteine-deprivation- or xCT-inhibition-induced ferroptosis. Additionally, we observed that levels of GPx4 protein are increased in OPA1-depleted cells, both under baseline conditions and during both erastin-induced and RSL3-induced ferroptosis. Our data show that these increases in GPx4 protein are dependent on induction of xCT in OPA1-depleted cells, consistent with prior ob-

servations that increased cysteine availability augments GPx4 translation.⁴¹ The observed increases in GPx4 protein levels provides an explanation as to why OPA1 loss protects against not only cysteine deprivation or xCT inhibition-induced ferroptosis but also against ferroptosis induced by direct pharmacological inhibition of GPx4 by RSL3. Given that elevations in GPx4 protein levels in OPA1-depleted cells are comparable in the contexts of both of these sets of ferroptosis inducers, the fact that OPA1 loss is ultimately less protective against GPx4 inhibition as compared with xCT inhibition suggests, again, that the differential OPA1 dependence of mitochondrial lipid ROS generation elicited by xCT inhibition versus RSL3 inhibition may be responsible.

Our data demonstrate that the upregulation of the xCT-GSH-GPx4 pathway is dependent on increases in *Slc7a11* transcription. Thus, RNA-seq was performed to further understand the transcriptomic landscape that could mediate this effect. Our IPA of RNA-seq data revealed ATF4, an activator of the integrated stress response, as a top upstream transcriptional regulator activated in *Opa1*^{-/-} MEFs, which is consistent with previous studies showing that mitochondrial stress, caused by inhibition of OXPHOS, mitochondrial DNA damage, or proteotoxicity, can trigger an integrated stress response.^{52,69,70} Indeed, knockdown of ATF4 reversed increases in ferroptosis-suppressing genes, including *Slc7a11*, and resensitized *Opa1*^{-/-} MEFs to ferroptosis, indicating that the ATF4-mediated integrated stress response serves as the molecular link between OPA1 loss and the upregulation of the xCT-GSH-GPx4 pathway. These findings are in keeping with studies demonstrating that metabolic stresses, including glucose starvation or OXPHOS inhibition, can curtail ferroptosis induction through adaptive mechanisms.^{49,71,72} Early in the discovery of ferroptosis, Dixon et al., showed that erastin can activate aspects of the ATF4-mediated integrated stress response, but the exact role of ATF4 in ferroptosis was not explored in detail.⁵⁴ Subsequent studies revealed that ATF4 induction can upregulate anti-ferroptosis programs to suppress ferroptosis.^{48–50,73} However, in contrast, Kalkavan et al. recently reported that drug-resistant cancer cells are sensitized toward ferroptosis in an ATF4-dependent manner.⁷⁴ These directionally divergent sets of observations are consistent with the current concept that, although ATF4 generally elicits a pro-survival stress response, the integrated stress response can also become maladaptive and induce cell death, perhaps in response to excessive or prolonged exposure to unfavorable conditions.⁷⁵ Therefore, whether ATF4 induction acts as a ferroptosis-inhibiting or ferroptosis-promoting mechanism likely depends on the cellular and environmental context.

Using unbiased lipidomics, we found that OPA1 affects the remodeling of a wide variety of lipid classes, including PLs, lysoPLs, GLs, free FAs, and SpLs. The increase in GLs, in particular triacylglycerols, is consistent with the findings of a previous study showing accumulation of triacylglycerols in *Opa1*^{-/-} MEFs.⁶⁰ The enrichment of free FAs in *Opa1*^{-/-} MEFs supports an alternative

(L and M) (L) Cell death assessed with SYTOX Green staining and (M) lipid peroxidation assessed with C-11 BODIPY staining in the indicated MEF cell lines treated with erastin (2 μ M).

(N and O) (N) Cell death and (O) lipid peroxidation in the indicated MEF cell lines treated with RSL3 (0.4 μ M). All data represent mean \pm SEM; $n = 3$ independent experiments. Statistical analysis was performed using two-tailed Student's *t* test or one-way ANOVA. * $p < 0.05$, ** $p < 0.01$, *** $p < 0.001$, **** $p < 0.0001$.

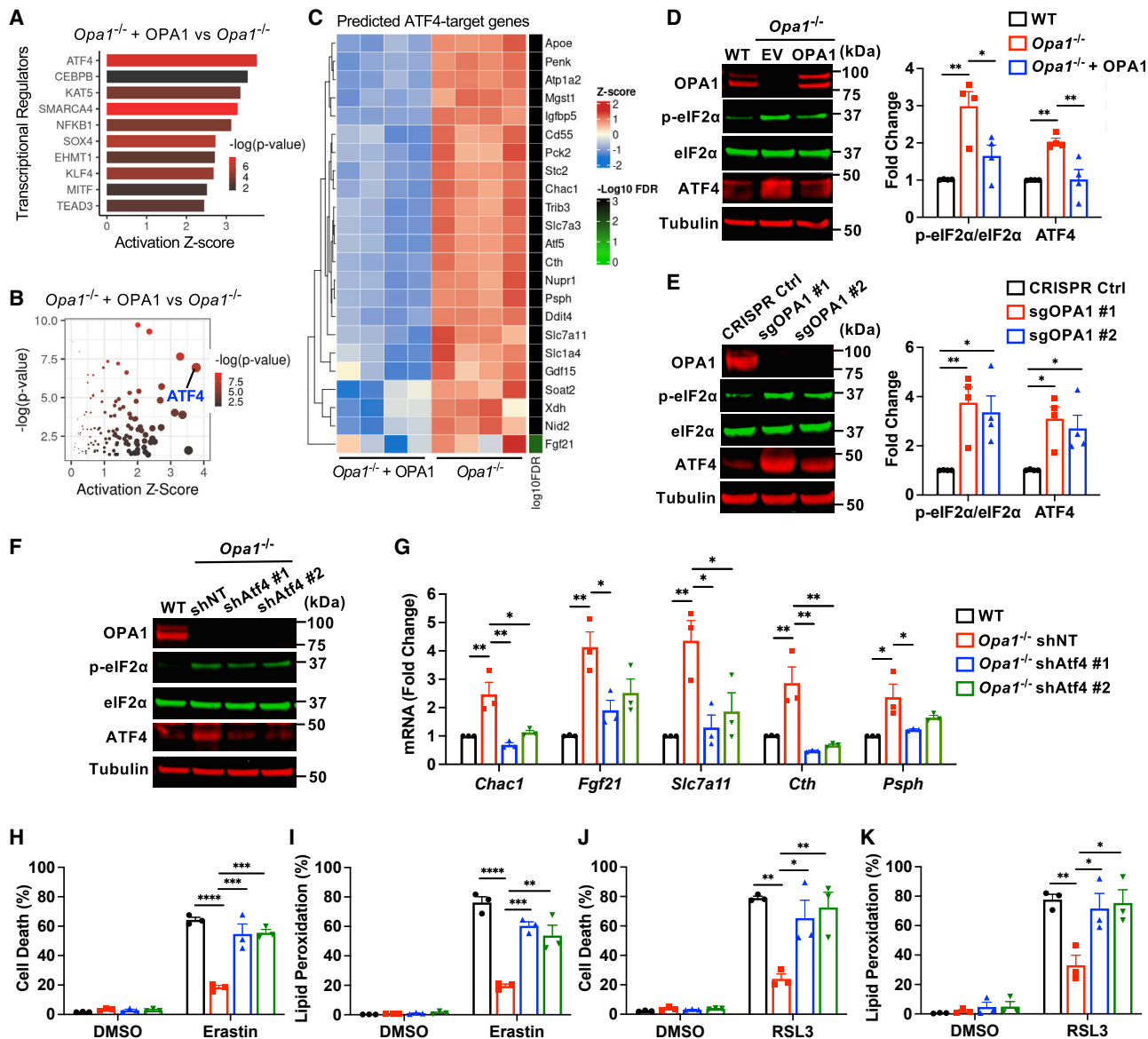


Figure 6. Ferroptosis-resistant state promoted by OPA1 loss is dependent on an ATF4-mediated integrated stress response

(A) Top ten induced transcriptional regulators determined by ingenuity pathway analysis in *Opa1*^{-/-} + OPA1 versus *Opa1*^{-/-} MEFs.

(B) Bubble plot showing ATF4 as an upstream regulator in *Opa1*^{-/-} + OPA1 versus *Opa1*^{-/-} MEFs.

(C) Heatmap of differentially expressed genes predicted to be ATF4 target genes.

(D and E) Immunoblot showing increases in p-eIF2α and ATF4 in (D) MEFs and (E) *Opa1*-deleted U2OS cells.

(F) Immunoblot of ATF4 following knockdown in *Opa1*^{-/-} MEFs.

(G) mRNA levels of ATF4-regulated genes in the indicated MEF cell lines.

(H and I) (H) Cell death assessed with SYTOX Green staining and (I) lipid peroxidation assessed with C-11 BODIPY staining in the indicated MEF cell lines treated with erastin (2 μM).

(J and K) (J) Cell death and (K) lipid peroxidation measured in indicated MEF cell lines treated with RSL3 (0.4 μM). All data represent mean ± SEM; n = at least 3 independent experiments. Statistical analysis was performed using two-tailed Student's t test or one-way ANOVA. *p < 0.05, **p < 0.01, ***p < 0.001, ****p < 0.0001.

function of OPA1 in activating lipolysis, as characterized by the Tasken group.⁵⁹ Loss of OPA1 also resulted in differential abundance of PUFA-PL subtypes compared with WT cells but, more intriguingly, MUFA-PLs, the lipid inhibitors of ferroptosis, were more enriched in *Opa1*^{-/-} MEFs. This raises the possibility that

accumulation of MUFA-PLs in *Opa1*^{-/-} MEFs may act in conjunction with induction of the xCT-GSH-GPx4 pathway and inhibition of mitochondrial lipid ROS to provide additional protection from ferroptosis, but this hypothesis requires further investigation. It is unclear precisely how the composition of PLs is regulated by OPA1. A

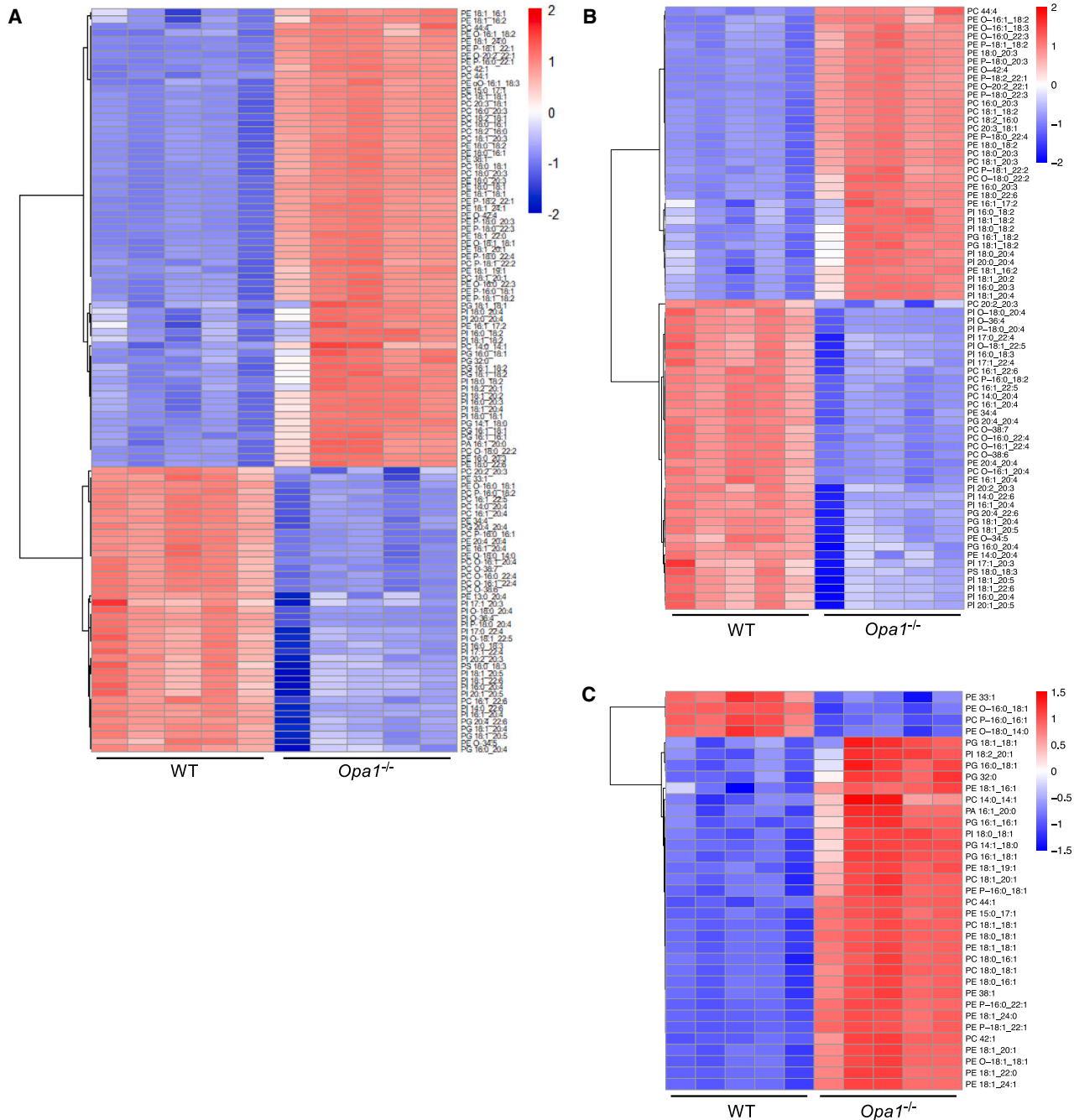


Figure 7. OPA1 regulates remodeling of phospholipids associated with ferroptosis susceptibility

(A) Heatmaps of significantly changed phospholipids.

(B) Heatmaps of significantly changed polyunsaturated fatty-acid-containing phospholipids (PUFA-PLs).

(C) Heatmaps of significantly changed monounsaturated fatty-acid-containing phospholipids (MUFA-PLs). Scale corresponds to FDR-corrected $p < 0.05$ with fold change threshold = 2.

recently published study showed that OPA1 mediates proximity of mitochondria and ER contact sites (MERCs) in an ATF4-dependent manner.⁷⁶ MERCs provide trafficking sites for transfer of calcium, lipids, proteins, and metabolites between the two organelles

that are essential for cellular function.^{77,78} Therefore, OPA1-dependent remodeling of PLs may occur through modulation of lipid transfer and biosynthesis mediated by MERCs, implicating a mitochondria-ER crosstalk.

OPA1 plays an important role in maintaining normal physiological function *in vivo*^{79–81}; however, inhibition of OPA1 may be beneficial in certain pathological contexts. In skeletal muscle, *Opa1* deficiency prevents age-induced and diet-induced obesity and insulin resistance⁸² and, in the liver, depletion of OPA1 ameliorates liver damage in nonalcoholic steatohepatitis (NASH)^{83,84} and protects against acetaminophen-induced toxicity.⁷⁰ Because ferroptosis has been implicated in the development of NASH and drug-induced liver failure,^{85,86} it is possible that the beneficial outcomes of OPA1 inhibition in the liver are associated with ferroptosis suppression. As such, OPA1 holds promise as a potential therapeutic target for ferroptosis inhibition in relevant diseases. Recent studies have also shown that OPA1 is required for tumor growth in xenograft models^{87–89} and that OPA1 overexpression enables cancer cells to acquire an OXPHOS-dependent resistance to chemotherapies.^{90,91} Moreover, in several human malignancies, including breast and pancreatic cancers, higher OPA1 expression is correlated with poor prognosis and patient survival.^{87,92} Given our data showing OPA1 as a positive regulator of ferroptosis, drug-resistant cancers that are highly dependent on OPA1-controlled metabolism may be more susceptible to ferroptosis. In such cases, high expression of OPA1 might serve as a predictive biomarker for the cancer's responsiveness to ferroptosis-targeted therapy. In contrast, downregulation of OPA1 in cancer cells may be an oncogenic tactic to evade ferroptosis induced by cell-intrinsic signals or anti-tumor immunity. Furthermore, upregulation of xCT or ATF4, which we demonstrate in OPA1-depleted cells, has been shown to support tumorigenesis by enabling cancer cell survival in hypoxic or nutrient-deprived microenvironments.^{75,93}

In conclusion, our studies unravel an OPA1-dependent cell state that links mitochondrial homeostasis to ferroptosis susceptibility. This dependency involves distinct mechanisms that include mitochondria's intrinsic ability in generating ROS via OXPHOS and extrinsic signaling with the nucleus to activate an ATF4-mediated integrated stress response. Although the GTPase activity is required for OPA1 to sensitize cells to ferroptosis, ferroptosis occurs independently of OPA1-mediated mitochondrial fusion. These findings provide a deeper understanding of the regulatory network linking mitochondrial structure-function and ferroptotic cell death that may guide future therapeutic efforts to mitigate or trigger ferroptosis in various disease states.

Limitations of the study

We have demonstrated that OPA1 promotes ferroptosis in both mouse and human cells, but additional studies will be required to explore the role of OPA1-mediated ferroptosis *in vivo*, including in the various disease paradigms discussed above. Second, we show that OPA1 is necessary for mitochondrial ROS generation during ferroptosis induced by cysteine deprivation or xCT inhibition with erastin, but not by direct GPx4 inhibition with RSL3. Additional studies will be needed to define what are likely distinct mechanisms of mitochondrial ROS generation in different contexts of ferroptosis induction. Finally, our lipidomics analysis has identified several OPA1-dependent lipid signatures, the functional importance of which—with respect to ferroptosis sensitivity—will require further investigation.

STAR★METHODS

Detailed methods are provided in the online version of this paper and include the following:

- KEY RESOURCES TABLE
- RESOURCE AVAILABILITY
 - Lead contact
 - Materials availability
 - Data and code availability
- EXPERIMENTAL MODEL AND STUDY PARTICIPANT DETAILS
 - Cell culture
- METHOD DETAILS
 - Lentivirus production and transduction
 - General cloning
 - Cell death assays
 - Lipid peroxidation measurements
 - Mitochondrial ROS and lipid ROS measurements
 - Mitochondrial morphology analysis by confocal microscopy
 - Seahorse assay for OCR measurements
 - Electron microscopy
 - Glutamate release assay
 - Glutathione measurements
 - Western blotting
 - RNA extraction and RT-PCR
 - RNA-sequencing and analysis
 - Lipidomics
- QUANTIFICATION AND STATISTICAL ANALYSIS

SUPPLEMENTAL INFORMATION

Supplemental information can be found online at <https://doi.org/10.1016/j.molcel.2024.07.020>.

ACKNOWLEDGMENTS

We note with sadness the recent passing of Dr. Yisang Yoon, who will be deeply missed by the scientific community. F.G.L. was supported by NIH training grant T32HL144456. J.L.A. was supported by NIH training grant T32GM007491 and American Heart Association Predoctoral Fellowship 837832. Y.Y. was supported by NIH grants R01HL093671 and R21EY031483. B.R.S. was supported by NIH grant R35CA209896. R.N.K. was supported by NIH grants R01HL159062, R01HL157319, and R01HL164772 and DOD grant PR191593. Biorender was used to generate the graphical abstract.

AUTHOR CONTRIBUTIONS

Conceptualization, F.G.L. and R.N.K.; methodology, F.G.L.; investigation, F.G.L., F.Z., J.L., J.L.A., and R.P.; formal analysis, F.G.L., F.Z., and J.L.A.; resources, Y.Y.; writing – original draft, F.G.L. and R.N.K.; writing – review and editing, F.G.L. and R.N.K.; visualization, F.G.L.; supervision, B.R.S. and R.N.K.; funding acquisition, R.N.K.

DECLARATION OF INTERESTS

B.R.S. is an inventor on patents and patent applications involving ferroptosis; co-founded and serves as a consultant to ProJenX, Inc. and Exarta Therapeutics; holds equity in Sonata Therapeutics; and serves as a consultant to Weatherwax Biotechnologies Corporation and Akin Gump Strauss Hauer & Feld LLP.

Received: June 19, 2023

Revised: May 22, 2024

Accepted: July 19, 2024

Published: August 13, 2024

REFERENCES

- Dixon, S.J., Lemberg, K.M., Lamprecht, M.R., Skouta, R., Zaitsev, E.M., Gleason, C.E., Patel, D.N., Bauer, A.J., Cantley, A.M., Yang, W.S., et al. (2012). Ferroptosis: an iron-dependent form of nonapoptotic cell death. *Cell* 149, 1060–1072. <https://doi.org/10.1016/j.cell.2012.03.042>.
- Dixon, S.J., and Stockwell, B.R. (2019). The hallmarks of ferroptosis. *Annu. Rev. Cancer Biol.* 3, 35–54. <https://doi.org/10.1146/annurev-cancerbio.2019.03.001>.
- Stockwell, B.R., Jiang, X., and Gu, W. (2020). Emerging mechanisms and disease relevance of ferroptosis. *Trends Cell Biol.* 30, 478–490. <https://doi.org/10.1016/j.tcb.2020.02.009>.
- Jiang, X., Stockwell, B.R., and Conrad, M. (2021). Ferroptosis: mechanisms, biology and role in disease. *Nat. Rev. Mol. Cell Biol.* 22, 266–282. <https://doi.org/10.1038/s41580-020-00324-8>.
- Lei, G., Zhuang, L., and Gan, B. (2022). Targeting ferroptosis as a vulnerability in cancer. *Nat. Rev. Cancer* 22, 381–396. <https://doi.org/10.1038/s41568-022-00459-0>.
- Yang, W.S., SriRamaratnam, R., Welsch, M.E., Shimada, K., Skouta, R., Viswanathan, V.S., Cheah, J.H., Clemons, P.A., Shamji, A.F., Clish, C.B., et al. (2014). Regulation of ferroptotic cancer cell death by GPX4. *Cell* 156, 317–331. <https://doi.org/10.1016/j.cell.2013.12.010>.
- Seiler, A., Schneider, M., Förster, H., Roth, S., Wirth, E.K., Culmsee, C., Plesnila, N., Kremmer, E., Rådmark, O., Wurst, W., et al. (2008). Glutathione peroxidase 4 senses and translates oxidative stress into 12/15-lipoxygenase dependent- and AIF-mediated cell death. *Cell Metab.* 8, 237–248. <https://doi.org/10.1016/j.cmet.2008.07.005>.
- Stockwell, B.R., Friedmann Angeli, J.P., Bayir, H., Bush, A.I., Conrad, M., Dixon, S.J., Fulda, S., Gascón, S., Hatzios, S.K., Kagan, V.E., et al. (2017). Ferroptosis: A regulated cell death nexus linking metabolism, redox biology, and disease. *Cell* 171, 273–285. <https://doi.org/10.1016/j.cell.2017.09.021>.
- Conrad, M., and Sato, H. (2012). The oxidative stress-inducible cystine/glutamate antiporter, system x (c) (-): cystine supplier and beyond. *Amino Acids* 42, 231–246. <https://doi.org/10.1007/s00726-011-0867-5>.
- Poltorack, C.D., and Dixon, S.J. (2022). Understanding the role of cysteine in ferroptosis: progress & paradoxes. *FEBS Journal* 289, 374–385. <https://doi.org/10.1111/febs.15842>.
- Doll, S., Freitas, F.P., Shah, R., Aldrovandi, M., da Silva, M.C., Ingold, I., Goya Grocin, A., Xavier da Silva, T.N., Panzilius, E., Scheel, C.H., et al. (2019). FSP1 is a glutathione-independent ferroptosis suppressor. *Nature* 575, 693–698. <https://doi.org/10.1038/s41586-019-1707-0>.
- Bersuker, K., Hendricks, J.M., Li, Z., Magtanong, L., Ford, B., Tang, P.H., Roberts, M.A., Tong, B., Maimone, T.J., Zoncu, R., et al. (2019). The CoQ oxidoreductase FSP1 acts parallel to GPX4 to inhibit ferroptosis. *Nature* 575, 688–692. <https://doi.org/10.1038/s41586-019-1705-2>.
- Kraft, V.A.N., Bezjian, C.T., Pfeiffer, S., Ringelstetter, L., Müller, C., Zandkarimi, F., Merl-Pham, J., Bao, X., Anastasov, N., Kössl, J., et al. (2020). GTP cyclohydrolase 1/tetrahydrobiopterin counteract ferroptosis through lipid remodeling. *ACS Cent. Sci.* 6, 41–53. <https://doi.org/10.1021/acscentsci.9b01063>.
- Stockwell, B.R. (2022). Ferroptosis turns 10: Emerging mechanisms, physiological functions, and therapeutic applications. *Cell* 185, 2401–2421. <https://doi.org/10.1016/j.cell.2022.06.003>.
- Chen, X., Kang, R., Kroemer, G., and Tang, D. (2021). Organelle-specific regulation of ferroptosis. *Cell Death Differ.* 28, 2843–2856. <https://doi.org/10.1038/s41418-021-00859-z>.
- von Krusenstiern, A.N., Robson, R.N., Qian, N., Qiu, B., Hu, F., Reznik, E., Smith, N., Zandkarimi, F., Estes, V.M., Dupont, M., et al. (2023). Identification of essential sites of lipid peroxidation in ferroptosis. *Nat. Chem. Biol.* 19, 719–730. <https://doi.org/10.1038/s41589-022-01249-3>.
- Murphy, M.P. (2009). How mitochondria produce reactive oxygen species. *Biochem. J.* 417, 1–13. <https://doi.org/10.1042/BJ20081386>.
- Finkel, T. (2011). Signal transduction by reactive oxygen species. *J. Cell Biol.* 194, 7–15. <https://doi.org/10.1083/jcb.2011102095>.
- Friedmann Angeli, J.P., Schneider, M., Proneth, B., Tyurina, Y.Y., Tyurin, V.A., Hammond, V.J., Herbach, N., Aichler, M., Walch, A., Eggenhofer, E., et al. (2014). Inactivation of the ferroptosis regulator Gpx4 triggers acute renal failure in mice. *Nat. Cell Biol.* 16, 1180–1191. <https://doi.org/10.1038/ncb3064>.
- Jelinek, A., Heyder, L., Daude, M., Plessner, M., Krippner, S., Grosse, R., Diederich, W.E., and Culmsee, C. (2018). Mitochondrial rescue prevents glutathione peroxidase-dependent ferroptosis. *Free Radic. Biol. Med.* 117, 45–57. <https://doi.org/10.1016/j.freeradbiomed.2018.01.019>.
- Oh, S.J., Ikeda, M., Ide, T., Hur, K.Y., and Lee, M.S. (2022). Mitochondrial event as an ultimate step in ferroptosis. *Cell Death Discov.* 8, 414. <https://doi.org/10.1038/s41420-022-01199-8>.
- Krainz, T., Gaschler, M.M., Lim, C., Sacher, J.R., Stockwell, B.R., and Wipf, P. (2016). A mitochondrial-targeted nitroxide is a potent inhibitor of ferroptosis. *ACS Cent. Sci.* 2, 653–659. <https://doi.org/10.1021/acscentsci.6b00199>.
- Fang, X., Wang, H., Han, D., Xie, E., Yang, X., Wei, J., Gu, S., Gao, F., Zhu, N., Yin, X., et al. (2019). Ferroptosis as a target for protection against cardiomyopathy. *Proc. Natl. Acad. Sci. USA* 116, 2672–2680. <https://doi.org/10.1073/pnas.1821022116>.
- Tadokoro, T., Ikeda, M., Ide, T., Deguchi, H., Ikeda, S., Okabe, K., Ishikita, A., Matsushima, S., Koumura, T., Yamada, K.I., et al. (2020). Mitochondria-dependent ferroptosis plays a pivotal role in doxorubicin cardiotoxicity. *JCI Insight* 5, e132747. <https://doi.org/10.1172/jci.insight.132747>.
- Mao, C., Liu, X., Zhang, Y., Lei, G., Yan, Y., Lee, H., Koppula, P., Wu, S., Zhuang, L., Fang, B., et al. (2021). DHODH-mediated ferroptosis defence is a targetable vulnerability in cancer. *Nature* 593, 586–590. <https://doi.org/10.1038/s41586-021-03539-7>.
- Wu, S., Mao, C., Kondiparthi, L., Poyurovsky, M.V., Olszewski, K., and Gan, B. (2022). A ferroptosis defense mechanism mediated by glycerol-3-phosphate dehydrogenase 2 in mitochondria. *Proc. Natl. Acad. Sci. USA* 119, e2121987119. <https://doi.org/10.1073/pnas.2121987119>.
- Deshwal, S., Onishi, M., Tatsuta, T., Bartsch, T., Cors, E., Ried, K., Lemke, K., Nolte, H., Giavalisco, P., and Langer, T. (2023). Mitochondria regulate intracellular coenzyme Q transport and ferroptotic resistance via STARD7. *Nat. Cell Biol.* 25, 246–257. <https://doi.org/10.1038/s41556-022-01071-y>.
- MacVicar, T., and Langer, T. (2016). OPA1 processing in cell death and disease - the long and short of it. *J. Cell Sci.* 129, 2297–2306. <https://doi.org/10.1242/jcs.159186>.
- Quintana-Cabrera, R., and Scorrano, L. (2023). Determinants and outcomes of mitochondrial dynamics. *Mol. Cell* 83, 857–876. <https://doi.org/10.1016/j.molcel.2023.02.012>.
- Cipolat, S., Martins de Brito, O., Dal Zilio, B., and Scorrano, L. (2004). OPA1 requires mitofusin 1 to promote mitochondrial fusion. *Proc. Natl. Acad. Sci. USA* 101, 15927–15932. <https://doi.org/10.1073/pnas.0407043101>.
- Lee, H., Smith, S.B., and Yoon, Y. (2017). The short variant of the mitochondrial dynamin OPA1 maintains mitochondrial energetics and cristae structure. *J. Biol. Chem.* 292, 7115–7130. <https://doi.org/10.1074/jbc.M116.762567>.
- Del Dotto, V., Mishra, P., Vidoni, S., Fogazza, M., Maresca, A., Caporali, L., McCaffery, J.M., Cappelletti, M., Baruffini, E., Lenaers, G., et al. (2017). OPA1 isoforms in the hierarchical organization of mitochondrial functions. *Cell Rep.* 19, 2557–2571. <https://doi.org/10.1016/j.celrep.2017.05.073>.
- Giacomello, M., Pyakurel, A., Glytsou, C., and Scorrano, L. (2020). The cell biology of mitochondrial membrane dynamics. *Nat. Rev. Mol. Cell Biol.* 21, 204–224. <https://doi.org/10.1038/s41580-020-0210-7>.
- Doll, S., Proneth, B., Tyurina, Y.Y., Panzilius, E., Kobayashi, S., Ingold, I., Irmiler, M., Beckers, J., Aichler, M., Walch, A., et al. (2017). ACSL4 dictates ferroptosis sensitivity by shaping cellular lipid composition. *Nat. Chem. Biol.* 13, 91–98. <https://doi.org/10.1038/nchembio.2239>.

35. Neitemeier, S., Jelinek, A., Laino, V., Hoffmann, L., Eisenbach, I., Eying, R., Ganjam, G.K., Dolga, A.M., Oppermann, S., and Culmsee, C. (2017). BID links ferroptosis to mitochondrial cell death pathways. *Redox Biol.* *12*, 558–570. <https://doi.org/10.1016/j.redox.2017.03.007>.
36. Delettre, C., Griffoin, J.M., Kaplan, J., Dollfus, H., Lorenz, B., Faivre, L., Lenaers, G., Belenguer, P., and Hamel, C.P. (2001). Mutation spectrum and splicing variants in the OPA1 gene. *Hum. Genet.* *109*, 584–591. <https://doi.org/10.1007/s00439-001-0633-y>.
37. Song, Z., Chen, H., Fiket, M., Alexander, C., and Chan, D.C. (2007). OPA1 processing controls mitochondrial fusion and is regulated by mRNA splicing, membrane potential, and Yme1L. *J. Cell Biol.* *178*, 749–755. <https://doi.org/10.1083/jcb.200704110>.
38. Ge, Y., Shi, X., Boopathy, S., McDonald, J., Smith, A.W., and Chao, L.H. (2020). Two forms of Opa1 cooperate to complete fusion of the mitochondrial inner-membrane. *eLife* *9*, e50973. <https://doi.org/10.7554/eLife.50973>.
39. Lee, H., and Yoon, Y. (2018). Mitochondrial membrane dynamics-functional positioning of OPA1. *Antioxidants (Basel)* *7*, 186. <https://doi.org/10.3390/antiox7120186>.
40. Gao, M., Yi, J., Zhu, J., Minikes, A.M., Monian, P., Thompson, C.B., and Jiang, X. (2019). Role of mitochondria in ferroptosis. *Mol. Cell* *73*, 354–363.e3. <https://doi.org/10.1016/j.molcel.2018.10.042>.
41. Zhang, Y., Swanda, R.V., Nie, L., Liu, X., Wang, C., Lee, H., Lei, G., Mao, C., Koppula, P., Cheng, W., et al. (2021). mTORC1 couples cyst(e)ine availability with GPX4 protein synthesis and ferroptosis regulation. *Nat. Commun.* *12*, 1589. <https://doi.org/10.1038/s41467-021-21841-w>.
42. Wu, Z., Geng, Y., Lu, X., Shi, Y., Wu, G., Zhang, M., Shan, B., Pan, H., and Yuan, J. (2019). Chaperone-mediated autophagy is involved in the execution of ferroptosis. *Proc. Natl. Acad. Sci. USA* *116*, 2996–3005. <https://doi.org/10.1073/pnas.1819728116>.
43. Liu, H., Forouhar, F., Seibt, T., Saneto, R., Wigby, K., Friedman, J., Xia, X., Shchepinov, M.S., Ramesh, S.K., Conrad, M., et al. (2022). Characterization of a patient-derived variant of GPX4 for precision therapy. *Nat. Chem. Biol.* *18*, 91–100. <https://doi.org/10.1038/s41589-021-00915-2>.
44. Liu, J., Kuang, F., Kroemer, G., Klionsky, D.J., Kang, R., and Tang, D. (2020). Autophagy-dependent ferroptosis: machinery and regulation. *Cell Chem. Biol.* *27*, 420–435. <https://doi.org/10.1016/j.chembiol.2020.02.005>.
45. Pereira, R.O., Marti, A., Olvera, A.C., Tadinada, S.M., Bjorkman, S.H., Weatherford, E.T., Morgan, D.A., Westphal, M., Patel, P.H., Kirby, A.K., et al. (2021). OPA1 deletion in brown adipose tissue improves thermoregulation and systemic metabolism via FGF21. *eLife* *10*, e66519. <https://doi.org/10.7554/eLife.66519>.
46. Herkenne, S., Ek, O., Zamberlan, M., Pellattiero, A., Chergova, M., Chivite, I., Novotná, E., Rigoni, G., Fonseca, T.B., Samardzic, D., et al. (2020). Developmental and tumor angiogenesis requires the mitochondria-shaping protein Opa1. *Cell Metab.* *31*, 987–1003.e8. <https://doi.org/10.1016/j.cmet.2020.04.007>.
47. Tezze, C., Romanello, V., Desbats, M.A., Fadini, G.P., Albiero, M., Favaro, G., Ciciliot, S., Soriano, M.E., Morbidoni, V., Cerqua, C., et al. (2017). Age-associated loss of OPA1 in muscle impacts muscle mass, metabolic homeostasis, systemic inflammation, and epithelial senescence. *Cell Metab.* *25*, 1374–1389.e6. <https://doi.org/10.1016/j.cmet.2017.04.021>.
48. Gao, R., Kalathur, R.K.R., Coto-Llerena, M., Ercan, C., Buechel, D., Shuang, S., Piscuoglio, S., Dill, M.T., Camargo, F.D., Christofori, G., et al. (2021). YAP/TAZ and ATF4 drive resistance to sorafenib in hepatocellular carcinoma by preventing ferroptosis. *EMBO Mol. Med.* *13*, e14351. <https://doi.org/10.15252/emmm.202114351>.
49. Ahola, S., Rivera Mejias, P., Hermans, S., Chandragiri, S., Giavalisco, P., Nolte, H., and Langer, T. (2022). OMA1-mediated integrated stress response protects against ferroptosis in mitochondrial cardiomyopathy. *Cell Metab.* *34*, 1875–1891.e7. <https://doi.org/10.1016/j.cmet.2022.08.017>.
50. He, F., Zhang, P., Liu, J., Wang, R., Kaufman, R.J., Yaden, B.C., and Karin, M. (2023). ATF4 suppresses hepatocarcinogenesis by inducing SLC7A11 (xCT) to block stress-related ferroptosis. *J. Hepatol.* *79*, 362–377. <https://doi.org/10.1016/j.jhep.2023.03.016>.
51. Pakos-Zebrucka, K., Koryga, I., Mnich, K., Ljujic, M., Samali, A., and Gorman, A.M. (2016). The integrated stress response. *EMBO Rep.* *17*, 1374–1395. <https://doi.org/10.15252/embr.201642195>.
52. Quirós, P.M., Prado, M.A., Zamboni, N., D’Amico, D., Williams, R.W., Finley, D., Gygi, S.P., and Auwerx, J. (2017). Multi-omics analysis identifies ATF4 as a key regulator of the mitochondrial stress response in mammals. *J. Cell Biol.* *216*, 2027–2045. <https://doi.org/10.1083/jcb.201702058>.
53. Torrence, M.E., MacArthur, M.R., Hosios, A.M., Valvezan, A.J., Asara, J.M., Mitchell, J.R., and Manning, B.D. (2021). The mTORC1-mediated activation of ATF4 promotes protein and glutathione synthesis downstream of growth signals. *eLife* *10*, e63326. <https://doi.org/10.7554/eLife.63326>.
54. Dixon, S.J., Patel, D.N., Welsch, M., Skouta, R., Lee, E.D., Hayano, M., Thomas, A.G., Gleason, C.E., Tatonetti, N.P., Slusher, B.S., et al. (2014). Pharmacological inhibition of cystine-glutamate exchange induces endoplasmic reticulum stress and ferroptosis. *eLife* *3*, e02523. <https://doi.org/10.7554/eLife.02523>.
55. Hayano, M., Yang, W.S., Corn, C.K., Pagano, N.C., and Stockwell, B.R. (2016). Loss of cysteinyl-tRNA synthetase (CARS) induces the transsulfuration pathway and inhibits ferroptosis induced by cystine deprivation. *Cell Death Differ.* *23*, 270–278. <https://doi.org/10.1038/cdd.2015.93>.
56. Guo, X., Aviles, G., Liu, Y., Tian, R., Unger, B.A., Lin, Y.T., Wiita, A.P., Xu, K., Correia, M.A., and Kampmann, M. (2020). Mitochondrial stress is relayed to the cytosol by an OMA1-DELE1-HRI pathway. *Nature* *579*, 427–432. <https://doi.org/10.1038/s41586-020-2078-2>.
57. Yoon, H., Shaw, J.L., Haigis, M.C., and Greka, A. (2021). Lipid metabolism in sickness and in health: emerging regulators of lipotoxicity. *Mol. Cell* *81*, 3708–3730. <https://doi.org/10.1016/j.molcel.2021.08.027>.
58. Ban, T., Ishihara, T., Kohno, H., Saita, S., Ichimura, A., Maenaka, K., Oka, T., Mihara, K., and Ishihara, N. (2017). Molecular basis of selective mitochondrial fusion by heterotypic action between OPA1 and cardiolipin. *Nat. Cell Biol.* *19*, 856–863. <https://doi.org/10.1038/ncb3560>.
59. Pidoux, G., Witczak, O., Jarnæss, E., Myrvold, L., Urlaub, H., Stokka, A.J., Küntziger, T., and Taskén, K. (2011). Optic atrophy 1 is an A-kinase anchoring protein on lipid droplets that mediates adrenergic control of lipolysis. *EMBO J.* *30*, 4371–4386. <https://doi.org/10.1038/emboj.2011.365>.
60. Bocca, C., Kane, M.S., Veyrat-Durebex, C., Nzoughe, J.K., Chao de la Barca, J.M., Chupin, S., Alban, J., Procaccio, V., Bonneau, D., Simard, G., et al. (2019). Lipidomics reveals triacylglycerol accumulation due to impaired fatty acid flux in Opa1-disrupted fibroblasts. *J. Proteome Res.* *18*, 2779–2790. <https://doi.org/10.1021/acs.jproteome.9b00081>.
61. Pereira, R.O., Olvera, A.C., Marti, A., Fang, S., White, J.R., Westphal, M., Hewezi, R., AshShareef, S.T., García-Peña, L.M., Koneru, J., et al. (2022). OPA1 regulates lipid metabolism and cold-induced browning of White adipose tissue in mice. *Diabetes* *71*, 2572–2583. <https://doi.org/10.2337/db22-0450>.
62. Yang, W.S., Kim, K.J., Gaschler, M.M., Patel, M., Shchepinov, M.S., and Stockwell, B.R. (2016). Peroxidation of polyunsaturated fatty acids by lipoygenases drives ferroptosis. *Proc. Natl. Acad. Sci. USA* *113*, E4966–E4975. <https://doi.org/10.1073/pnas.1603244113>.
63. Dixon, S.J., and Pratt, D.A. (2023). Ferroptosis: A flexible constellation of related biochemical mechanisms. *Mol. Cell* *83*, 1030–1042. <https://doi.org/10.1016/j.molcel.2023.03.005>.
64. Magtanong, L., Ko, P.J., To, M., Cao, J.Y., Forcina, G.C., Tarangelo, A., Ward, C.C., Cho, K., Patti, G.J., Nomura, D.K., et al. (2019). Exogenous monounsaturated fatty acids promote a ferroptosis-resistant cell state. *Cell Chem. Biol.* *26*, 420–432.e9. <https://doi.org/10.1016/j.chembiol.2018.11.016>.

65. Frezza, C., Cipolat, S., Martins de Brito, O., Micaroni, M., Beznoussenko, G.V., Rudka, T., Bartoli, D., Polishuck, R.S., Danial, N.N., De Strooper, B., et al. (2006). OPA1 controls apoptotic cristae remodeling independently from mitochondrial fusion. *Cell* 126, 177–189. <https://doi.org/10.1016/j.cell.2006.06.025>.
66. Lee, H., Smith, S.B., Sheu, S.S., and Yoon, Y. (2020). The short variant of optic atrophy 1 (OPA1) improves cell survival under oxidative stress. *J. Biol. Chem.* 295, 6543–6560. <https://doi.org/10.1074/jbc.RA119.010983>.
67. Baker, N., Wade, S., Triolo, M., Girgis, J., Chwastek, D., Larrigan, S., Feige, P., Fujita, R., Crist, C., Rudnicki, M.A., et al. (2022). The mitochondrial protein OPA1 regulates the quiescent state of adult muscle stem cells. *Cell Stem Cell* 29, 1315–1332.e9. <https://doi.org/10.1016/j.stem.2022.07.010>.
68. Khacho, M., Clark, A., Svoboda, D.S., Azzi, J., MacLaurin, J.G., Meghaizel, C., Sesaki, H., Lagace, D.C., Germain, M., Harper, M.E., et al. (2016). Mitochondrial dynamics impacts stem cell identity and fate decisions by regulating a nuclear transcriptional program. *Cell Stem Cell* 19, 232–247. <https://doi.org/10.1016/j.stem.2016.04.015>.
69. Mick, E., Titov, D.V., Skinner, O.S., Sharma, R., Jourdain, A.A., and Mootha, V.K. (2020). Distinct mitochondrial defects trigger the integrated stress response depending on the metabolic state of the cell. *eLife* 9, e49178. <https://doi.org/10.7554/eLife.49178>.
70. Lee, H., Lee, T.J., Galloway, C.A., Zhi, W., Xiao, W., de Mesy Bentley, K.L., Sharma, A., Teng, Y., Sesaki, H., and Yoon, Y. (2023). The mitochondrial fusion protein OPA1 is dispensable in the liver and its absence induces mitohormesis to protect liver from drug-induced injury. *Nat. Commun.* 14, 6721. <https://doi.org/10.1038/s41467-023-42564-0>.
71. Lee, H., Zandkarimi, F., Zhang, Y., Meena, J.K., Kim, J., Zhuang, L., Tyagi, S., Ma, L., Westbrook, T.F., Steinberg, G.R., et al. (2020). Energy-stress-mediated AMPK activation inhibits ferroptosis. *Nat. Cell Biol.* 22, 225–234. <https://doi.org/10.1038/s41556-020-0461-8>.
72. Conlon, M., Poltorack, C.D., Forcina, G.C., Armenta, D.A., Mallais, M., Perez, M.A., Wells, A., Kahanu, A., Magtanong, L., Watts, J.L., et al. (2021). A compendium of kinetic modulatory profiles identifies ferroptosis regulators. *Nat. Chem. Biol.* 17, 665–674. <https://doi.org/10.1038/s41589-021-00751-4>.
73. Kang, L., Wang, D., Shen, T., Liu, X., Dai, B., Zhou, D., Shen, H., Gong, J., Li, G., Hu, Y., et al. (2023). PDIA4 confers resistance to ferroptosis via induction of ATF4/SLC7A11 in renal cell carcinoma. *Cell Death Dis.* 14, 193. <https://doi.org/10.1038/s41419-023-05719-x>.
74. Kalkavan, H., Chen, M.J., Crawford, J.C., Quarato, G., Fitzgerald, P., Tait, S.W.G., Goding, C.R., and Green, D.R. (2022). Sublethal cytochrome c release generates drug-tolerant persister cells. *Cell* 185, 3356–3374.e22. <https://doi.org/10.1016/j.cell.2022.07.025>.
75. Wortel, I.M.N., van der Meer, L.T., Kilberg, M.S., and van Leeuwen, F.N. (2017). Surviving stress: modulation of ATF4-mediated stress responses in normal and malignant cells. *Trends Endocrinol. Metab.* 28, 794–806. <https://doi.org/10.1016/j.tem.2017.07.003>.
76. Hinton, A., Jr., Katti, P., Mungai, M., Hall, D.D., Koval, O., Shao, J., Vue, Z., Lopez, E.G., Rostami, R., Neikirk, K., et al. (2024). ATF4-dependent increase in mitochondrial-endoplasmic reticulum tethering following OPA1 deletion in skeletal muscle. *J. Cell. Physiol.* 239, e31204. <https://doi.org/10.1002/jcp.31204>.
77. Naon, D., and Scorrano, L. (2014). At the right distance: ER-mitochondria juxtaposition in cell life and death. *Biochim. Biophys. Acta* 1843, 2184–2194. <https://doi.org/10.1016/j.bbamcr.2014.05.011>.
78. Silva, B.S.C., DiGiovanni, L., Kumar, R., Carmichael, R.E., Kim, P.K., and Schrader, M. (2020). Maintaining social contacts: the physiological relevance of organelle interactions. *Biochim. Biophys. Acta Mol. Cell Res.* 1867, 118800. <https://doi.org/10.1016/j.bbamcr.2020.118800>.
79. Chen, H., and Chan, D.C. (2017). Mitochondrial dynamics in regulating the unique phenotypes of cancer and stem cells. *Cell Metab.* 26, 39–48. <https://doi.org/10.1016/j.cmet.2017.05.016>.
80. Chan, D.C. (2020). Mitochondrial dynamics and its involvement in disease. *Annu. Rev. Pathol.* 15, 235–259. <https://doi.org/10.1146/annurev-pathmechdis-012419-032711>.
81. Noone, J., O’Gorman, D.J., and Kenny, H.C. (2022). OPA1 regulation of mitochondrial dynamics in skeletal and cardiac muscle. *Trends Endocrinol. Metab.* 33, 710–721. <https://doi.org/10.1016/j.tem.2022.07.003>.
82. Pereira, R.O., Tadinada, S.M., Zasadny, F.M., Oliveira, K.J., Pires, K.M.P., Olvera, A., Jeffers, J., Souvenir, R., McGlaufflin, R., Seei, A., et al. (2017). OPA1 deficiency promotes secretion of FGF21 from muscle that prevents obesity and insulin resistance. *EMBO J.* 36, 2126–2145. <https://doi.org/10.15252/embj.201696179>.
83. Yamada, T., Murata, D., Adachi, Y., Itoh, K., Kameoka, S., Igarashi, A., Kato, T., Araki, Y., Haganir, R.L., Dawson, T.M., et al. (2018). Mitochondrial stasis reveals p62-mediated ubiquitination in parkin-independent mitophagy and mitigates nonalcoholic fatty liver disease. *Cell Metab.* 28, 588–604.e5. <https://doi.org/10.1016/j.cmet.2018.06.014>.
84. Yamada, T., Murata, D., Kleiner, D.E., Anders, R., Rosenberg, A.Z., Kaplan, J., Hamilton, J.P., Aghajan, M., Levi, M., Wang, N.-Y., et al. (2022). Prevention and regression of megamitochondria and steatosis by blocking mitochondrial fusion in the liver. *iScience* 25, 103996. <https://doi.org/10.1016/j.isci.2022.103996>.
85. Tsurusaki, S., Tsuchiya, Y., Koumura, T., Nakasone, M., Sakamoto, T., Matsuoka, M., Imai, H., Yuet-Yin Kok, C., Okochi, H., Nakano, H., et al. (2019). Hepatic ferroptosis plays an important role as the trigger for initiating inflammation in nonalcoholic steatohepatitis. *Cell Death Dis.* 10, 449. <https://doi.org/10.1038/s41419-019-1678-y>.
86. Yamada, N., Karasawa, T., Kimura, H., Watanabe, S., Komada, T., Kamata, R., Sampilvanjil, A., Ito, J., Nakagawa, K., Kuwata, H., et al. (2020). Ferroptosis driven by radical oxidation of n-6 polyunsaturated fatty acids mediates acetaminophen-induced acute liver failure. *Cell Death Dis.* 11, 144. <https://doi.org/10.1038/s41419-020-2334-2>.
87. Zamberlan, M., Boeckx, A., Muller, F., Vinelli, F., Ek, O., Vianello, C., Coart, E., Shibata, K., Christian, A., Grespi, F., et al. (2022). Inhibition of the mitochondrial protein Opa1 curtails breast cancer growth. *J. Exp. Clin. Cancer Res.* 41, 95. <https://doi.org/10.1186/s13046-022-02304-6>.
88. Liu, Z., Lei, J., Wu, T., Hu, W., Zheng, M., Wang, Y., Song, J., Ruan, H., Xu, L., Ren, T., et al. (2023). Lipogenesis promotes mitochondrial fusion and maintains cancer stemness in human NSCLC. *JCI Insight* 8, e158429. <https://doi.org/10.1172/jci.insight.158429>.
89. Li, M., Wang, L., Wang, Y., Zhang, S., Zhou, G., Lieshout, R., Ma, B., Liu, J., Qu, C., Verstegen, M.M.A., et al. (2020). Mitochondrial fusion via OPA1 and MFN1 supports liver tumor cell metabolism and growth. *Cells* 9, 121. <https://doi.org/10.3390/cells9010121>.
90. Chen, X., Glytsou, C., Zhou, H., Narang, S., Reyna, D.E., Lopez, A., Sakellaropoulos, T., Gong, Y., Kloetgen, A., Yap, Y.S., et al. (2019). Targeting mitochondrial structure sensitizes acute myeloid leukemia to Venetoclax treatment. *Cancer Discov.* 9, 890–909. <https://doi.org/10.1158/2159-8290.CD-19-0117>.
91. Noguchi, M., Kohno, S., Pellattiero, A., Machida, Y., Shibata, K., Shintani, N., Kohno, T., Gotoh, N., Takahashi, C., Hirao, A., et al. (2023). Inhibition of the mitochondria-shaping protein Opa1 restores sensitivity to gefitinib in a lung adenocarcinoma-resistant cell line. *Cell Death Dis.* 14, 241. <https://doi.org/10.1038/s41419-023-05768-2>.
92. Wee, Y., Liu, Y., Lu, J., Li, X., and Zhao, M. (2018). Identification of novel prognosis-related genes associated with cancer using integrative network analysis. *Sci. Rep.* 8, 3233. <https://doi.org/10.1038/s41598-018-21691-5>.
93. Koppula, P., Zhuang, L., and Gan, B. (2021). Cystine transporter SLC7A11/xCT in cancer: ferroptosis, nutrient dependency, and cancer therapy. *Protein Cell* 12, 599–620. <https://doi.org/10.1007/s13238-020-00789-5>.

STAR★METHODS

KEY RESOURCES TABLE

REAGENT or RESOURCE	SOURCE	IDENTIFIER
Antibodies		
Mouse monoclonal anti-OPA1	BD Biosciences	Cat# 612606; RRID: AB_399888
Mouse monoclonal anti-DRP1	BD Biosciences	Cat# 611739; RRID: AB_399215
Rabbit monoclonal anti-GPx4	Abcam	Cat# ab125066; RRID: AB_10973901
Rabbit polyclonal anti-FSP1	Proteintech	Cat# 20886-1-AP; RRID: AB_2878756
Rabbit polyclonal anti-DHODH	Proteintech	Cat# 14877-1-AP; RRID: AB_2091723
Rabbit polyclonal anti-STARD7	Proteintech	Cat# 15689-1-AP; RRID: AB_2197820
Rabbit monoclonal anti-phospho-eIF2 α	Cell Signaling	Cat# 3398; RRID: AB_2096481
Rabbit monoclonal anti-eIF2 α	Cell Signaling	Cat# 5324; RRID: AB_10692650
Mouse monoclonal anti-ATF4	Santa Cruz Biotechnology	Cat# sc-390063; RRID: AB_2810998
Mouse monoclonal anti- α -Tubulin	Sigma-Aldrich	Cat# T6074; RRID: AB_477582
Rabbit monoclonal anti-NDUFS1	Abcam	Cat# ab169540; RRID: AB_2687932
Mouse monoclonal anti-SDHA	Abcam	Cat# ab14715; RRID: AB_301433
Mouse monoclonal anti-UQCRC1	Sigma-Aldrich	Cat# SAB2702301
Rabbit polyclonal anti-Cox IV	Cell Signaling	Cat# 4844; RRID: AB_2085427
Rabbit polyclonal anti-ATPB	Abcam	Cat# ab128743; RRID: AB_2810299
Bacterial and virus strains		
NEB Stable Competent <i>E. Coli</i>	New England Biolabs	Cat# C3040H
Chemicals, peptides, and recombinant proteins		
Erastin	Cayman Chemicals	Cat# 17754
(1S,3R)-RSL3	Cayman Chemicals	Cat# 19288
Ferostatin-1	Cayman Chemicals	Cat# 17729
SYTOX Green Nucleic Acid Stain	Thermo Fisher Scientific	Cat# S7020
NucBlue Live ReadyProbes Reagent	Thermo Fisher Scientific	Cat# R37605
BODIPY 581/591 C11	Thermo Fisher Scientific	Cat# D3861
MitoPerOx	Cayman Chemicals	Cat# 18798
MitoSox	Thermo Fisher Scientific	Cat# M36008
MitoTracker Deep Red	Thermo Fisher Scientific	Cat# M22426
Tetramethylrhodamine, Ethyl Ester, Perchlorate (TMRE)	Thermo Fisher Scientific	Cat# T669
X-tremeGENE HD	Sigma-Aldrich	Cat# XTGHP-RO
Lenti-X Concentrator	Takara Bio Inc	Cat# 631232
T4 Polynucleotide Kinase	New England Biolabs	Cat# M0201L
Bsmbl-v2	New England Biolabs	Cat# R0739L
T4 DNA Ligase	New England Biolabs	Cat# M0202L
Critical commercial assays		
Glutamate-Glo Assay	Promega	Cat# J7021
CellTiter-Blue Cell Viability Assay	Promega	Cat# G8081
Glutathione Assay Kit	Cayman Chemicals	Cat# 703002
RNAeasy Plus Kit	Qiagen	Cat# 74134
Superscript IV VILO Kit	Thermo Fisher Scientific	Cat# 11756050
Power SYBR Green Master Mix	Thermo Fisher Scientific	Cat# 4367659
CyQuant Cell Proliferation Assay	Thermo Fisher Scientific	Cat# C7026

(Continued on next page)

REAGENT or RESOURCE	SOURCE	IDENTIFIER
Continued		
Deposited data		
RNA sequencing	This study	GSE269167
Lipidomic data	This study	MTBLS10544
Western blots and microscopy images	This study	https://doi.org/10.17632/cp8cvzx22z.1
Experimental models: Cell lines		
WT MEFs	ATCC	Cat# CRL-2991; RRID: CVCL_L690
Opa1 ^{-/-} MEFs	ATCC	Cat# CRL-2995
HEK293T	ATCC	Cat# CRL-3216
U2OS CRISPR Ctrl	This study	N/A
U2OS sgOPA1 #1	This study	N/A
U2OS sgOPA1 #2	This study	N/A
Oligonucleotides		
Refer to Table S1	This study	Table S1
Recombinant DNA		
pMD2.G	Addgene	Cat# 12259
psPAX2	Addgene	Cat# 12260
gag/pol	Addgene	Cat# 14887
pMSCV-empty vector	Addgene	Cat# 68469
pMSCV-OPA1 WT	Addgene	Cat# 26047
pMSCV-OPA1 K301A	Lee et al. ³¹	N/A
pMSCV-L-OPA1 (isoform 1ΔS1)	Song et al. ³⁷	N/A
pMSCV-S-OPA1 (isoform 5)	Song et al. ³⁷	N/A
LentiCRISPRv2	Addgene	Cat# 52961
LentiCRISPRv2 non-targeting gRNA	This study	N/A
LentiCRISPRv2 human OPA1 gRNA #1	This study	N/A
LentiCRISPRv2 human OPA1 gRNA #2	This study	N/A
Control shRNA	Addgene	Cat# 1864
Mission mouse Slc7a11 shRNA #1	Sigma-Aldrich	Cat# TRCN0000079426
Mission mouse Slc7a11 shRNA #2	Sigma-Aldrich	Cat# TRCN0000079427
Mission mouse Atf4 shRNA #1	Sigma-Aldrich	Cat# TRCN0000301721
Mission mouse Atf4 shRNA #2	Sigma-Aldrich	Cat# TRCN0000071726
Mission mouse Oma1 shRNA	Sigma-Aldrich	Cat# TRCN0000031080
Mission mouse Dele1 shRNA	Sigma-Aldrich	Cat# TRCN0000179419
Mission mouse Hri shRNA	Sigma-Aldrich	Cat# TRCN0000235940
Software and algorithms		
ImageJ	National Institutes of Health	RRID: SCR_003070; https://imagej.net/ij/
Prism v9	GraphPad	RRID: SCR_002798; https://www.graphpad.com/
Seahorse XF Cell Mito Stress Test Report Generator	Agilent	https://www.agilent.com/en/product/cell-analysis/real-time-cell-metabolic-analysis/xf-software/seahorse-xf-cell-mito-stress-test-report-generators-740899
FlowJo	FlowJo, LLC	RRID: SCR_008520; https://www.flowjo.com/
MetaboAnalyst v5	MetaboAnalyst software	RRID: SCR_015539; https://www.metaboanalyst.ca/
R	R project	RRID: SCR_001905; https://www.r-project.org/
Other		
DMEM	Thermo Fisher Scientific	Cat# 11965092
FluoroBrite DMEM	Thermo Fisher Scientific	Cat# A1896702
DMEM no glutamine, methionine, and cysteine	Thermo Fisher Scientific	Cat# 21013024
McCoy's 5A Medium	Thermo Fisher Scientific	Cat# 16600082

RESOURCE AVAILABILITY

Lead contact

Further information and requests for resources and reagents should be directed to and will be fulfilled by the lead contact, Richard N. Kitsis (richard.kitsis@einsteinmed.edu).

Materials availability

All unique reagents generated by this study are available from the [lead contact](#) either without restriction or with a completed Materials Transfer Agreement.

Data and code availability

- RNA-seq data has been deposited at GEO and will be publicly available as of the date of publication. Accession numbers are listed in the [key resources table](#). Lipidomic data has been deposited at MetaboLights and will be publicly available as of the date of publication. Accession numbers are listed in the [key resources table](#). Western blots and microscopy images have been deposited in Mendeley Data will be publicly available as of the date of publication. The DOI is listed in the [key resources table](#).
- This study did not produce any original code.
- Any additional information required to reanalyze the data reported in this paper is available from the [lead contact](#) upon request.

EXPERIMENTAL MODEL AND STUDY PARTICIPANT DETAILS

Cell culture

WT MEFs, *Opa1*^{-/-} MEFs and HEK293Ts were cultured in Dulbecco's Modified Eagle's Medium (DMEM) supplemented with 10% (v/v) FBS, 2 mM L-glutamine, and 100 units/mL penicillin/100 ug/mL streptomycin. U2OS cells were cultured in McCoy's 5A Medium supplemented with 10% (v/v) FBS and 100 units/mL penicillin/100 ug/mL streptomycin. All cells were cultured in a 37°C incubator in presence of 5% CO₂.

METHOD DETAILS

Lentivirus production and transduction

To produce lentivirus, packaging vectors pMD2.G (Addgene) and psPAX2 (Addgene) were used. To produce retrovirus, packaging vectors pMD2.G (Addgene) and gag/pol (Addgene) were used. HEK293T cells were transfected with packaging vectors and insert vector using X-tremeGENE HD (Sigma-Aldrich) according to the manufacturer's protocol. Supernatant was collected and concentrated using Lenti-X Concentrator (Takara Bio Inc) and stored at -80°C until ready to use. MEFs and U2OS were infected with either lentivirus or retrovirus containing 0.8 ug/mL polybrene. Beginning 48 h post-infection, MEFs and U2OS were subjected to puromycin (2.5 ug/mL) treatment for 4 d to eliminate un-infected cells.

General cloning

Oligonucleotides encoding non-targeting and OPA1 targeting guide sequences were cloned into the lentiCRISPRv2 construct. LentiCRISPRv2 was digested with Bsmbl-v2 (NEB) and sgRNA oligonucleotides were annealed with T4 Polynucleotide Kinase (NEB). Hybridized oligonucleotides were ligated into Bsmbl-digested lentiCRISPRv2 with T4 DNA Ligase (NEB). Ligation products were transformed into NEB Stable Competent *E. Coli* and plasmids were purified from bacterial cultures. Non-targeting and OPA1 targeting gRNA sequences in the lentiCRISPRv2 construct was confirmed by sanger sequencing.

Cell death assays

For flow cytometry, MEFs and U2OS cells were seeded at a density of 6x10⁴ and 5x10⁴ cells, respectively, per well in a 12-well plate and grown overnight before treatments. To induce ferroptosis, MEFs were treated with 2 μM erastin or 0.4 μM RSL3 for 24 h, and U2OS cells were treated with 10 μM erastin or 4 μM RSL3 for 36 h unless stated otherwise in figure legends. For cysteine withdrawal, culture medium was replaced with cystine-free DMEM for 24 and 26 hours for MEFs and U2OS cells, respectively. At the end of the indicated time points, cells were stained with 10 nM SYTOX Green for 15 min at room temperature and processed for flow cytometry. Cell death was determined by cells with green fluorescence at Ex/Em wavelengths of 488nm/525nm. Each biological group consists of three technical replicates and at least 10,000 events were analyzed per replicate. The data were analyzed using FlowJo Software.

For plate reader measurements, MEFs and U2OS cells were seeded at a density of 6x10³ and 5x10³ cells, respectively, per well in a 96-well plate, and grown overnight. The next day, culture medium was replaced with cystine-free DMEM for the indicated time points in the figure legend before the cells were stained with 10 nM SYTOX Green for 15 min at room temperature. Cell death was determined by total green fluorescent units per well. Each biological group consists of three technical replicates.

In experiments where microscopy images were taken, NucBlue Live ReadyProbes Reagent was added to stain for live and dead cells.

Lipid peroxidation measurements

MEFs were treated with cystine-free DMEM, 2 μM erastin or 0.4 μM RSL3 for 8 h to induce lipid peroxidation. U2OS cells were treated with cystine-free DMEM, 10 μM erastin or 4 μM RSL3 for 16 h to induce lipid peroxidation. Afterwards, cells were stained with 2 μM C-11 BODIPY for 30 min at 37°C and harvested for flow cytometry. Lipid peroxidation was determined in cells with green fluorescence at Ex/Em wavelengths of 488nm/525nm. Each biological group consists of three technical replicates and at least 10,000 events were analyzed per replicate. The data were analyzed using FlowJo Software.

Mitochondrial ROS and lipid ROS measurements

MEFs were treated with cystine-free DMEM, 2 μM erastin or 0.4 μM RSL3 for 8 h. For mitochondrial superoxide, cells were stained with 5 μM MitoSox Red for 10 min at 37°C. For mitochondrial lipid peroxidation, cells were stained with 200 nM MitoPerOx for 30 min at 37°C.

Cells were washed and harvested for flow cytometry. Mitochondrial superoxide and mitochondrial lipid peroxidation were determined at Ex/Em wavelengths of 510nm/610nm and 488nm/525nm, respectively. Each biological group consists of three technical replicates and at least 10,000 events were analyzed per replicate. The data were analyzed using FlowJo Software.

Mitochondrial morphology analysis by confocal microscopy

MEFs were seeded at a density of 2.5×10^5 cells in 35 mm glass bottom dishes (Matek Corporation). The next day, cells were stained with 250 nM Mitotracker Deep Red for 15 min at 37°C. After incubation, cells were washed with DPBS and placed in FluoroBrite DMEM supplemented with 10% (v/v) FBS, 2 mM L-glutamine, 100 units/mL penicillin/100 $\mu\text{g}/\text{mL}$ streptomycin and 10mM HEPES for imaging. Images were captured using a 100x oil objective on a confocal microscope (Nikon CSU-W1 Spinning Disk Confocal). Cells were classified into three categories based on their overall mitochondrial morphology: long tubular, short tubular or fragmented. At least 100 cells were counted per group in each experiment.

Seahorse assay for OCR measurements

MEFs were seeded at a density of 1×10^4 cells per well in Seahorse XF96 V3 PS cell culture microplate (Agilent, 101085-004) the day before seahorse assay. Prior to the start of assay, cells were incubated with an assay medium (XF DMEM supplemented with 1 mM pyruvate, 2 mM glutamine, 10 mM glucose) in a 37°C non-CO₂ incubator for 1 h. Standard assay conditions for seahorse were used, including injections of 1.5 μM oligomycin, 1 μM FCCP, 2 μM rotenone, 4 μM antimycin. Normalization to cell count was performed for each well using CyQuant Cell Proliferation Assay. OCR values were determined using Agilent's Seahorse XF Cell Mito Stress Test Report Generator.

Electron microscopy

MEFs were seeded in 60 mm plates and allowed to reach 80% confluency overnight. The next day, samples were fixed with 2.5% glutaraldehyde, 2% paraformaldehyde in 0.1 M cacodylate buffer and post-fixed with 1% osmium tetroxide followed by 2% uranyl acetate, dehydrated through a graded series of ethanol and embedded in LX112 resin (LADD Research Industries, Burlington VT). Ultrathin sections were cut on a Leica Ultracut UC7, stained with uranyl acetate followed by lead citrate and viewed on a JEOL 1400 Plus transmission electron microscope at 120kv.

Glutamate release assay

MEFs and U2OS cells were seeded at a density of 1×10^4 cells per well in a 96-well plate. The next day, cells were washed with PBS before being treated with 2 μM erastin (for MEFs) or 10 μM erastin (for U2OS) in FBS-free FluoroBrite DMEM. After 1 h incubation, glutamate release from cells were measured in the extracellular media using the Glutamate-Glo Assay (Promega). Glutamate levels were normalized to cell viability measured by the CellTiter-Blue Cell Viability Assay (Promega).

Glutathione measurements

MEFs were seeded at a density of 2.5×10^5 cells per well in a 6-well plate and grown overnight before treating with vehicle or 2 μM erastin the next day. U2OS cells were seeded at a density of 5×10^5 cells per well in a 60 mm plate and grown overnight before treating with vehicle or 10 μM erastin the next day. Cells were harvested by cell scraper and lysed by sonication. Glutathione levels were quantified using the Glutathione Assay Kit (Cayman Chemicals). Total levels of glutathione were normalized to protein concentrations as determined by Bradford's reagent.

Western blotting

SDS-PAGE

Cells were lysed using RIPA buffer supplemented with protease inhibitors. After centrifugation of cell debris, 30-40 μg of protein lysate was loaded for SDS-PAGE. For western blotting, PVDF membranes incubated with primary antibody overnight at 4°C followed

by secondary antibody at room temperature for 1 h. Primary antibodies used include OPA1 (BD Biosciences, 612606; 1:1000), DRP1 (BD Biosciences, 611739; 1:1000), GPx4 (Abcam, ab125066; 1:1000), FSP1 (Proteintech, 20886-1-AP; 1:1000), DHODH (Proteintech, 14877-1-AP; 1:1000), STARD7 (Proteintech, 15689-1-AP; 1:1000), phospho-eIF2 α (Cell Signaling, 3398; 1:1000), eIF2 α (Cell Signaling, 5324; 1:2000), ATF4 (Santa Cruz Biotechnology, sc-390063; 1:100), and α -Tubulin (Sigma-Aldrich, T6074; 1:5000).

BN-PAGE

Cells were harvested by scraper and suspended in sucrose buffer for lysis with dounce homogenizer. After removal of cell debris, mitochondria was isolated from total lysate by centrifugation at 10,000g for 15 min at 4°C. 30 μ g of mitochondria was permeabilized with extraction buffer (5% digitonin; 4x BN sample buffer; protease inhibitors; water) for 15 min and then centrifuged at 10,000 g for 10 min at 4°C. Supernatants containing mitochondrial supercomplexes were incorporated in LB buffer (5% G-250; 4x BN sample buffer; water) and loaded in blue native (BN) gel. For western blotting, PVDF membranes incubated with primary antibody overnight at 4°C followed by secondary antibody at room temperature for 1 h. Primary antibodies used include NDUFS1 (Abcam, ab169540; 1:5000), SDHA (Abcam, ab14715; 1:5000), UQCRC1 (Sigma-Aldrich, SAB2702301; 1:1000), Cox IV (Cell Signaling, 4844; 1:1000), and ATPB (Abcam, ab128743; 1:5000).

RNA extraction and RT-PCR

Total RNA was extracted from cultured cells using the RNeasy Plus Kit (Qiagen), according to the manufacturer's instructions. Total RNA was reverse transcribed into cDNA using the Superscript IV VILO Kit (Thermo Fisher Scientific). RT-PCR was performed with 25 ng of cDNA and Power SYBR Green Master Mix (Thermo Fisher Scientific) using standard conditions for comparative C_T on the ViiA 7 Real-Time PCR System. The house keeping gene, Rpl39, served as an internal control for normalization of target mRNA genes.

RNA-sequencing and analysis

Library preparation and Illumina sequencing

RNA processing and sequencing were outsourced to Azenta (MD, USA). Total RNA was extracted from cells using the RNeasy Mini Kit (Qiagen) following the manufacturer's instructions. After RNA integrity was checked using Agilent TapeStation 4200, RNA sequencing libraries were prepared using the NEBNext Ultra II RNA Library Prep Kit according to the manufacturer's instructions. mRNA were enriched with Oligod(T) beads and then fragmented for 15 min at 94°C. Next, cDNA were synthesized, ligated to universal adapters and amplified by PCR. Sequencing library quality and quantity was verified on the Agilent TapeStation and Qubit 4 Fluorometer, respectively. The library samples were subjected to two rounds of 150bp Paired End (PE) sequencing on the HiSeq 4000 (Illumina).

Data analysis

Illumina sequencing reads were de-multiplexed using Illumina's bcl2fastq 2.17 software. After raw data quality check and adapter removal, the trimmed reads were aligned to the mouse reference genome (GRCm38) on ENSEMBL using the STAR aligner v.2.5.2b. The estimated transcript counts were calculated using feature Counts of the Subread package v.1.5.2 from the BAM files. Differential gene expression analysis between the *Opa1*^{-/-} and *Opa1*^{-/-} + *Opa1* samples was performed using DESeq2. Genes with FDR adjusted *p* values < 0.05 and absolute log₂ fold change > 1 following the Wald test were considered as differentially expressed genes. For pathway analysis, we used Ingenuity Pathway Analysis software utilizing all differentially expressed genes.

Lipidomics

Sample preparation

MEFs (five independent biological replicates per condition) were seeded in 150 mm culture dishes at a density of 5x10⁶ per dish. The next day, the cells were washed with cold PBS (2x) and harvested using a cell scraper. Cell pellets were collected by centrifugation at 800 g and snap-frozen on dry ice before storing at -80°C. Lipids were extracted from each cell pellet as described previously.⁷¹ Briefly, samples were homogenized in ice-cold methanol containing SPLASH® LIPIDOMIX® Mass Spec Standard (Avanti Polar Lipids, Inc.) using glass bead homogenizer tubes. After homogenization, samples were transferred to fresh glass vials containing 850 μ l of cold methyl-tert-butyl ether and vortex-mixed for 30 s. Next, 200 μ l of ice-cold water was added, and the samples were incubated on ice for 20 min. After centrifugation (3,000 r.p.m. for 20 min at 4 °C), the lipid-containing upper phase was collected and dried down under a gentle stream of nitrogen gas. A mixture of 2-propanol/acetonitrile/water (4:3:1, v/v/v and 0.01% butylated hydroxytoluene) was used to reconstitute the dried samples before LC-MS analysis. A quality control sample (QC) was prepared by combining 50 μ l of each sample to assess the reproducibility of the features through the runs.

Liquid-chromatography-mass-spectrometry conditions

Lipids were separated using an Acquity UPLC CSH column (2.1 \times 100 mm, 1.7 μ m) over a 20-min gradient elution on a Waters Acquity UPLC I-Class system. Mobile phases A - acetonitrile/water (60:40, v/v) - and B - 2-propanol/acetonitrile/water (85:10:5, v/v/v) - contained 0.1% acetic acid and 10 mM ammonium acetate. Following the injections, the gradient was held at 40% mobile phase B for 2 min. At 2.1 min, it reached 50% B, then increased to 70% B in 12 min, at 12.1 min changed to 70% B and at 18 min increased to 99% B. The eluent composition returned to the initial condition in 1 min, and the column was re-equilibrated for an additional 1 min before the next injection was performed. The oven temperature was set at 55 °C and the flow rate was 400 μ l/min.

The SYNAPT G2-Si -Q-ToF mass spectrometer was operated in both positive and negative electrospray ionization modes. For the positive mode, a capillary voltage and sampling cone voltage of +2 kV and 32 V were used. The source and desolvation temperatures were kept at 120 and 500 °C, respectively. Nitrogen was used as the desolvation gas with a flow rate of 800L/h. For the negative mode, a capillary voltage of -1.5 kV and a cone voltage of 30 V was used. The source temperature was 120 °C, and the desolvation gas flow was set to 800 L/h. The data were collected in duplicates in data-independent (MS^E) mode over the mass range m/z : 50 to 1,200 Da. The quality control sample was also acquired in enhanced data-independent ion mobility (HDMSE) in both positive and negative modes for enhancing the structural assignment of lipid species. The electrospray ionization source settings for ion mobility were the same as described above. The traveling wave velocity was set to 650 m/s, and the wave height was 40 V. The helium gas flow in the helium cell region of the ion-mobility spectrometry cell was set to 180 mL/min. Nitrogen, used as the drift gas, was held at a flow rate of 95L/min in the ion-mobility spectrometry cell. The low collision energy was set to 4 eV, and the high collision energy was ramped from 25 to 65 eV in the transfer region of the T-Wave device to induce the fragmentation of mobility-separated precursor ions.

Data preprocessing and analysis

All of the raw files acquired via MassLynx software (Version 4.1, Waters) were imported to Progenesis Q1 software (Waters, Non-linear Dynamics) and aligned against the QC reference, followed by peak extraction and retention time alignment for each compound. The structural elucidation and validation of significant features were first obtained by searching monoisotopic masses against the Lipid MAPS (<https://www.lipidmaps.org/>) with a mass tolerance of 5 ppm. Fragment ion information obtained by tandem MS (UPLC-HDMSE) was used for the further structural elucidation of significantly changed lipid species. HDMSE data were processed using MSE data viewer (version 1.3, Waters Corp.). Multivariate statistical analyses and the heatmap were performed using MetaboAnalyst (version 5.0) and also in an R environment. Group differences were calculated using Welch's t test. p values were corrected for multiple hypothesis testing, and an FDR of 0.05 or less was considered significant.

QUANTIFICATION AND STATISTICAL ANALYSIS

Investigators were not blinded to the sample identities during data collection or analysis. All data are represented by at least 3 independent experiments. The quantified data with statistical analysis were performed using GraphPad Prism (v9) software. Unpaired two-sided Student's t test was used to compare two groups and one-way ANOVA was used to compare 3 or more groups. p values are indicated in figures and figure legends. $P < 0.05$ was considered statistically significant.